STEADY STATE HEAT TRANSFER CHARACTERIZATION OF A LIQUID METAL THERMAL SWITCH

By

TRAVIS SLOAN WISER

A thesis submitted in partial fulfillment of

the requirements for the degree of

Masters of Science in Mechanical Engineering

WASHINGTON STATE UNIVERSITY

School of Mechanical and Materials Engineering

AUGUST 2005

To the Faculty of Washington State University:

The members of the Committee appointed to examine the thesis of TRAVIS SLOAN WISER find it satisfactory and recommend that it be accepted.

_____
Chair

_____

_____

ACKNOWLEDGEMENT

First and foremost I would like to thank Dr. Robert Richards for his help with the research process and experimentation. The thesis presented here could not have been completed without his guidance. I would also like to thank Dr. Cill Richards and Dr. Bahr for their advice and expertise during the time I have been a P^3 member. The combination of knowledge and experience helped to expedite the research process.

I would also like to thank the following P^3 group members: Karl Olsen for his help increasing the accuracy and reliability of the test stand, Leland Weiss for helping with many aspects of my research including the modeling of heat transfer in a vacuum environment, Kevin Crain for his help with the droplet statistical analysis, and Jeong Cho for his help with mercury deposition which allowed me to focus on completing these experiments. Everyone in the P^3 group has affected my life and I am grateful for the experience I have had over the past two years.

STEADY STATE HEAT TRANSFER CHARACTERIZATION OF LIQUID METAL THERMAL SWITCH

Abstract
by Travis Sloan Wiser, M.S.
Washington State University
August 2005

Chair: Robert Richards

Steady state heat transfer characteristics have been quantified for a liquid metal thermal switch. The application motivating this research is the P^3 micro heat engine which converts heat energy into electrical power using the charge generating property of PZT. Stacks of engines are necessary to produce a useable charge and cyclic heating must be realized to make these stacks efficient.

The thermal switch consists of a silicon substrate with mercury micro-droplets deposited in a 1600 droplet array. Droplets are deposited using a vapor deposition process where mercury vapor preferentially condenses on 30 μm^2 gold pads sputtered on the silicon substrate. When the droplet arrays make contact with a second silicon substrate heat is transferred and the switch is "on". When the droplet arrays do not make contact, heat transfer across the resulting gas gap is sharply reduced and the switch is "off".

Three gas gaps are compared for the thermal switch. The reference condition is a gap filled with air at ambient pressure. The second condition is Xenon at ambient pressure. The third condition is air at a pressure of 0.5 torr.

The vacuum and xenon conditions reduce the transfer of heat in comparison with air when the switch is “off”. By reducing the heat transfer greater thermal isolation can be obtained at smaller gap distances.

The ideal switch would have minimal heat transfer in the “off” position and maximum heat transfer in the “on” position. A non-dimensional parameter the ratio of thermal resistance, “off” to “on”, is used to gauge the effectiveness of thermal switches. Xenon at ambient pressure has the best ratio of 143, when switching from 1 N load to 88 μm distance. This is followed by air at ambient pressure, 123, and air at 0.5 torr, 74. When switching from 1N to 22 μm distance the best ratio is obtained for air at 0.5 torr which is 60. This value followed by xenon at 50 and air at ambient pressure, 43.

TABLE OF CONTENTS

LIST OF TABLES

LIST OF FIGURES

Chapter 1 INTRODUCTION

Characterizing heat transfer in MEMS (microelectromechanical systems) allows the design to be more efficient and effective. Electronic packages are becoming smaller and the ability to reject heat faster becomes more important. Heat rejection is the limiting design constraint for minimizing the size of portable electronic devices. A micro heat engine has been developed by researchers at Washington State University [1,2]. This electronic package requires efficient heat input and rejection as well as the ability to control the duration of heat transfer. A micro thermal switch has been proposed to regulate the heat transfer in and out of the device [3]. The research presented in this thesis will expand on research conducted by Christensen [3] to include various environmental conditions.

1.1 MOTIVATION

The research presented in this thesis is motivated by the P^3 engine [1,2]. The P3 engine has been developed to provide a high energy density power source alternative to batteries. Batteries have a very low energy density in comparison with values for the P^3 engine. The P^3 engine will potentially provide a light weight alternative to batteries with the ability to harvest heat from a variety of heat sources.

The P^3 engine is fabricated using standard micromachining techniques. This is another advantage over electrochemical batteries. Thin piezoelectric/silicon membranes sealed together with a working fluid inside make up the heat engine. Piezoelectrics are distinguished by the property that an electric field is created when they are strained. Heat

is applied to the engine cavity and the working fluid expands and forms a vapor. The membrane expansion causes a strain in the PZT where a charge can be harvested.

A key element to the operation of the heat engine is the heat transfer in and out of the engine. A liquid-metal micro-droplet thermal switch has been developed for this application [3]. Since these are micro-devices one engine will produce a small amount of power. A cascade of engines must be assembled to provide adequate power for running devices such as cell phones and two-way radios. Heat transfer holds the key to unlocking the P^3 engines potential.

Heat must be transferred into the engine in a cyclic fashion to allow for large engine cascades and high engine efficiency. Continuous output of work by the engine can only be accomplished through a cyclic operation. Thermal flow is restricted and engine efficiency diminishes when engine is not operated cyclically. Constant heat addition reduces the expansion and contraction of the PZT covered membrane which reduces the quantity of power that can be harvested. To acquire cyclic heat transfer a micro heat switch has been designed. The switch consists of a Si substrate with mercury micro-droplets deposited on small gold pads [3]. The Si substrate allows the switch to be easily implemented into the engine cascade using standard micro-machining techniques while the mercury droplets reduce the amount of degradation caused by mechanical wear.

Figure 1.1 is a schematic of the thermal switch, used to control the flow of heat. The “on” position is when the heat source A is in contact with the heat sink B. The “off” position occurs when the heat source A and heat sink B are relatively far apart. The distance between hot and cold side of the switch and the interstitial fluid become critical parameters in regards to the “on” and “off” switching.

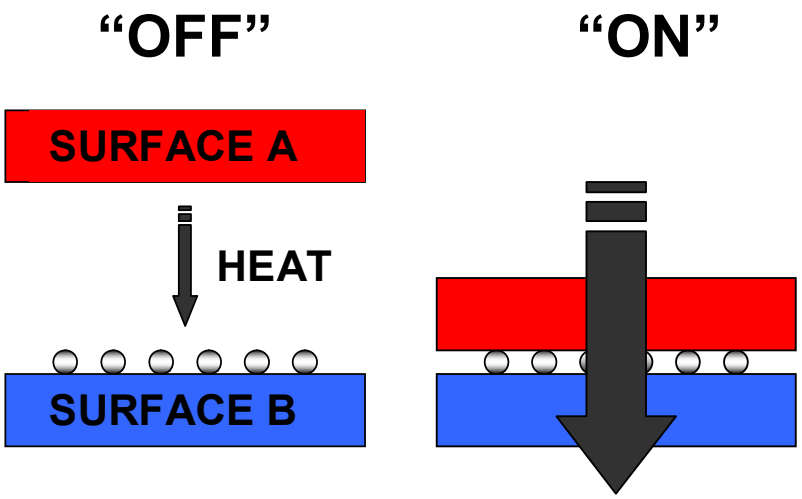

Figure 1.1: Schematic of “on” and “off” switch positions.

The “on” to “off” heat transfer ratio can be improved by changing parameters of the thermal switch. Since the conduction through air at small gap distances is 0.0263W/m•K it is reasonable to predict that changing the gas surrounding the switch to Xenon, conductivity of 0.00569W/m•K, would increase the heat transfer ratio[4]. Evacuation of the space between the thermal switch is another avenue which would increase the heat transfer ratio of the “off” and “on” positions. The engine membranes seal a refrigerant in the cavity which suggests it would be possible to fill the space between an engine and thermal switch with various fluids. The research presented in this paper will characterize the steady state heat transfer in the micro-droplet thermal switch for three different environmental conditions.

1.2 LITERATURE REVIEW

1.2.1 Thermal Conductance

Steady-state heat transfer measurements will be used to characterize the thermal switch in various mediums. Calibration of the apparatus consisted of measuring the thermal resistance of the Si substrate used in the mercury micro-droplet array to quantify the parallel heat path. Due to the wide variety of industrial applications of silicon there are many published articles on the measured thermal resistance.

Ruf [5] conducted a steady state heat transfer experiment which measured the thermal conductivity of a 10g single crystal of Silicon (99.8588% pure). Thermal resistance, K*m/W, and thermal conductivity, W/K*m are inversely related. Thermal conductivity measured 60% higher for a single crystal of Silicon than that of natural Si at room temperature. Dislocations and chemical impurities cause the large variation in thermal conductivity. Thin films also experience adverse affects of dislocations and chemical impurities in Silicon.

Amorphous hydrogenated silicon has many applications in solar cells and thin film transistor fabrication. The thermal conductivity of amorphous silicon thin films in one dimension using steady state heat transfer was measured because of these specialized applications [6]. Films were prepared with various amounts of disorder and hydrogen content. The researchers concluded that amorphous silicon thin films exhibit a low thermal conductivity due to presence of micro-porosities in the film network. The thermal conductivity is lowered in hydrogen-rich and highly disordered films which can be explained by phonon scattering due to increases in porosity size.

Porous silicon (PS) is are good candidate for thermal insulating layers. Porous silicon has a strong photoluminescence which suggests they could be used in optoelectronic applications. Other applications include sensors and devices that require high thermal insulation in order to obtain a large temperature variation with a small amount of heat input. Examples include; infrared sensors, bolometers, thermocouples, and thermal gas sensors. Many electronic devices using silicon based sensors require knowledge of thermal properties for conditioning power dissipation. Numerous ways to measure thermal resistance in these structures have been developed.

Prior to Volz [7] there was no technique for measuring the thermal conductance of porous Si due to the fragile nature of the material. The thermal conductivity of a 90% porosity silicon was measured using a thin Pt wire probe mounted in a scanning electron microscope where probe temperature is proportional to PS thermal resistance. Monocrystalline silicon (150 w/mK) has roughly a two order of magnitude higher thermal conductance than PS. Higher porosities result in lower thermal conductivities.

Photoacoustic (PA) techniques have also been developed to measure the thermal conductance of PS. The frequency variation of photacoustic signal in amplitude and phase was studied and thermal characteristics were quantified by means of a model which incorporates specific material properties. PA techniques are based on generation of thermal waves in test specimen by modulated light absorption [8,9]. Frequency of thermal waves corresponds with different layers of the test specimen.

Performance and reliability of high-density submicron electronic circuits, laser systems, sensors etc., composed of one or more thin layer of material, are highly dependent on the capability of the device to dispose of its internally generated heat. Thin

film SiO_2 thermal characteristics have been measured using a transient thermoreflectance system by Burzo[10]. Junctions between the Si and additional layers have a thermal resistance at least two times any of the thermal characteristics of the materials joined in the junction. Interfacial effects, including boundary resistance, and scattering of electrons and photons decrease the effective conductivity. Silicon oxides thermal conductivity is about 75% of the bulk value [10]. Deposition techniques heavily effect the thermal resistance which affects the ability of electronic devices to be cooled

A limiting criteria on micro-miniaturization of electronic components is acceptable junction temperature and thus an effective cooling device is necessary. Micro heat pipes have been developed to increase the cooling of Si wafers [11]. Micro-heat pipe arrays are etched into silicon wafers using anisotropic etching with KOH solution. The working fluid in the heat pipes is methanol. The micro-pipe array's effective thermal conductivity was measured by obtaining the temperature distribution along the longitudinal axis of the micro-heat pipe. This is similar to the device that the MEMS group at Washington State University is creating, however, in our device the frequency of the heat dissipation needs to be controlled.

Heat conduction interface has been studied using carbon nanotubes, grown on a silicon substrate [12], as the interstitial medium. One of the major goals in heat rejection of chip packages is reduction of interfacial, or contact resistance. Theory and experiments show extremely high phonon-dominated thermal conductivities, which are up to 5000-8000 W/m •K and 3000 W/m•K at room temperature for individual single-wall carbon nanotubes. The temperature of the device was measured using a infrared thermography. The minimum resistance of nanotube arrays were measured as 23-37

mm^2 •K/W under a pressure of 0.445 MPa [12]. The range of these values is most likely due to nanotube alignment, density, and length.

The thermal conductance of silicon independently, and also in combination with liquids, thin films, and nanotubes has many important applications in terms of electronic design. The research presented in this paper uses measured values of silicon resistance as a test stand calibration. Silicon is also used as a substrate for the thermal switch. While silicon conductance has been measured for various compositions, thicknesses, and combinations of materials the thermal conductance of mercury droplets on silicon substrate in various mediums and atmospheric conditions has not been studied. Numerous modeling techniques and experiments have been developed to measure thermal resistance of liquid mercury.

One technique that has been used to describe heat transfer through liquid mercury is a three layer model. The heat-pulse technique was used, which consists of measuring the diffusion time of a temperature pulse through a specimen. This technique has been widely used for measurements on single-layer solid specimens. It virtually eliminates thermal contact resistance and minimizes heat loss. A three layer model was solved for heat transfer through liquid mercury and results show a 7-11% discrepancy versus measured values which could be due to experimental error [13].

More recently thermal conductivities of silicone oil and mercury were measured using the hot-disk method in a short-duration microgravity environment by Nagai [14]. Motivation comes from difficulty of measuring the thermal conductivities of liquid materials because heat is transferred through convection as well as conduction. In micro gravity the thermal convection is suppressed, making thermal conductivity measurements

more precise. A 10 meter drop tower is used to provide the microgravity environment. Measurements were made for Hg on the ground to compare with measurements in microgravity. It was found that convection was suppressed in microgravity. Thermal conductivity of mercury in microgravity is about 3% lower than that on the ground around room temperature [14]. Another method for measuring thermal conductivity of liquids and powders involves the use of a thermistor probe in conjunction with numerical analysis.

Two dimensional heat conduction model of specimen including thermistor is developed and calculated numerically[15]. Conductivity of the specimen is determined by minimizing the difference between the numerical model and thermistor temperature histories. Thermal conductivity is determined by a small temperature rise over a short measurement time with small sample. This allows them to suppress the natural convection effect for liquids and redistribution of moisture for powders.

Many methods have been utilized to measure thermal conductance of the materials used in the experiment reported in this paper. The combination of material used to fabricate the thermal switch has been characterized only by Christensen and there has been no characterization of the thermal switch in various environmental conditions. The primary reason mercury micro-droplets were chosen is due to the increased compliance over a hard silicon switch and the ability for the liquid metal to reduce contact resistance.

1.2.2 Contact Resistance

When two surfaces are brought together an imperfect junction exists. Solid surfaces contain a large number of peaks and valleys which cause heat to transfer only at

discrete points on the surfaces, shown schematically in Figure 1.2. Thermophysical properties, characteristics of contacting surfaces, presence of interstitial material, and overall environment of the junction determine the temperature gradients experienced when materials contact [16]. Contact resistance is defined as:

$$R_{contact} = \frac{\Delta T}{q} \tag{1.1}$$

where: ΔT is the temperature difference between contacting surfaces

q is the heat transfer across interface

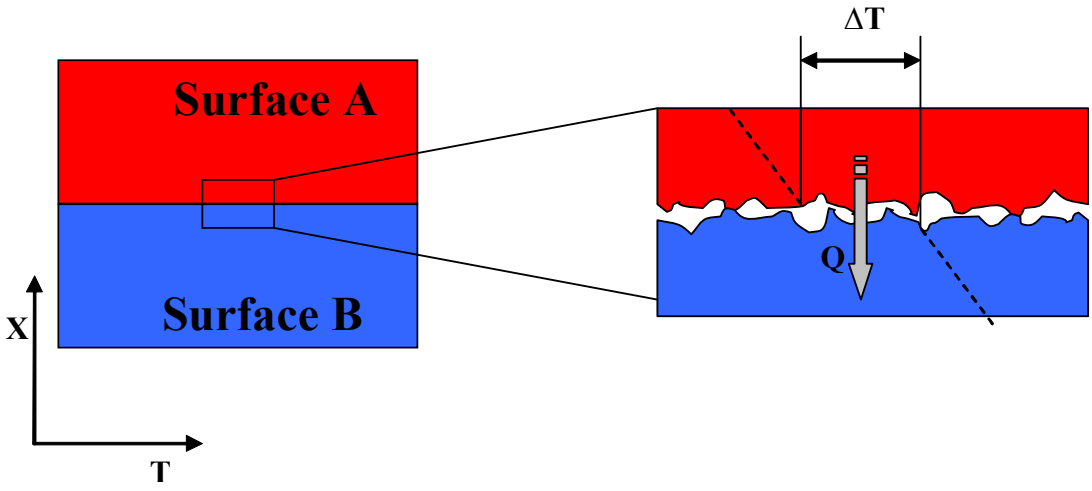

Figure 1.2: Schematic of contact resistance.

In absence of an interstitial medium heat is transferred across a interface by conduction through micro-contacts and also through radiation. Experiments were performed in vacuum for specimens of stainless steel, aluminum, and mild steel[17,18].

The effects of loading and unloading were analyzed by Li [17]. Contact conductance increases with an increase in applied pressure due to plastic deformation of micro-contacts. The area in contact increases as a larger load is applied and as number of loading cycles increases. For the stainless steel specimens the conductance was 33% higher for unloading compared with the loading phase. The mild steel samples saw an increase of 150% in the unloading phase compared to the loading phase. The number of loading cycles was also studied and it was found that after approximately 30 cycles there was no significant change in the contact conductance.

For low contact pressure applications the predominant mode of heat transfer across a joint is through the interstitial material, a gas-gap in most cases. Experiments were conducted for various surfaces finishes as well as several interstitial gases including mixtures [19]. It is assumed heat loss due to radiation is negligible below 300° C. The interstitial fluids used for these experiments were; helium, argon, carbon dioxide, nitrogen, and a mixtures of argon and helium. Specimens used were 304 stainless steel with polished contact surfaces. A simple relationship was found to exist between mean separation distance and surface roughness.

A macroscale contact conductance experiment was performed using packed beds of particles [20]. The materials evaluated include; Aluminum 2017-T4, Yellow Brass, Stainless Steel 304, and Chromium Alloy AiSI 52100. Data was collected in a vacuum of $5x10^{-5}$ Torr with applied pressure of 0.2-8.0 MPa. Thermocouples were located along

the axis of the column. The temperature of interface surfaces were determined by extrapolating measured temperatures along the fixture centerline. Heat flux was measured indirectly using the centerline temperatures therefore the test fixtures where constructed of materials whose thermal conductivities have been certified by the NIST (National Institute of Standards and Technology).

Contact conductance is the resistance to heat transfer at material interfaces due to their imperfect junction. The thermal switch being characterized in this research paper consists of microdroplets of mercury on a silicon substrate. Mercury droplets are used to increase contact conductance by conforming to the contacting surface.

1.2.3 Mercury Deposition

Mercury deposition has been performed for various applications. Mercury micro-droplets have been used in micromechanical electrical switches to heat switches[3,21].

The research of Be'er pertains to spreading of 150 micron mercury micro-droplet onto a Au substrate[22]. Growing interfaces are analyzed to determine roughness and growth exponents. Gold thin film thicknesses used are 1500 angstroms and 3000 angstroms.

Christensen developed the process used to deposit mercury onto silicon dies used at Washington State University [3]. This process allows us to deposit mercury droplets with diameters around 30 μm onto a silicon substrate with 30 μm^2 gold pads. The array size used in the experiments presented here are 40X40 arrays for a total of 1600 droplets.

1.2.4 Thermal Switches (Heat Switch)

Thermal switches are very similar to electrical switches however instead of turning power on and off thermal switches turn heat on and off. There are many applications for thermal switches especially in the field of space travel. Some types of thermal switches are: gas gap(single and multiple use), sorption gas gap, diode heat pipes, bi-metallic, and microelectromechanical thermal switches. Primarily these heat switches have been used in cryogenic applications which mean sub-zero temperatures.

Gas sorption thermal switches can be designed many ways. One such switch was constructed of two coaxial copper tubes with a 0.1 mm gap between them. The switch is operated by emitting and extracting He gas between the two cylinders of copper. A mini charcoal pump is used for adsorption and is controlled by electrical heat and a weak thermal link to a pumped He bath. The switch conductivity in the on position is 50 μW/K at 1.5 K. In the off state its conductivity is 8 mW/K at 0.5 K [23]. The switch is actuated within 10 seconds and takes as long as 10 minutes to turn off. Various materials can be used to change the pressure of the working fluid in a gas gap thermal switch.

Researchers at the California Institute of Technology are assessing the use of a Zr-V-Fe alloy as the actuator in gas-gap thermal switches. Properties of the "on" and "off" states are governed by the gap dimension, thermal conductivity of the gas, and properties of the surfaces. Hydrogen gas-gap switches have been used in high temperature batteries, sorption cryocoolers that produce cryogenic refrigeration, and other cryogenic applications. Research concluded that SAES Zr-V-Fe St-172 alloy is a viable candidate for use in actuators of gas-gap heat switches in sorption bed cryocoolers [24].

Thermal switches have been developed for enhancement of the Brilliant Eyes (BE) government baseline payload configuration for the Flight Demonstration System with infrared sensing capability with and without running a cryogenic refrigerator. BE is the lowest altitude of the U.S. Air-Force's space-based infrared surveillance and tracking system architecture. The switch thermally isolates two cooling systems. The primary infrared focal plane array is cooled by a pair of cryogenic refrigerators at 60K. The primary infrared focal plane array is used for both the tactical warning and attack assessment and ballistic missile defense missions. The co-located second focal plane assembly operates at a higher temperature and is passively cooled by a cryogenic radiator at 135 K. The secondary focal plane array is used for tactical warning and attack assessment missions only. The thermal switch allows the systems to be isolated. Without the switch the 65K refrigerators would be forced to cool the higher temperature radiator. The switch also provides redundant cooling capabilities which increases the sensor's reliability.

Study on the enhancement of the BE consisted of looking at multiple types of thermal switches and determining the gas-gap sorption bed was recommended as primary concept with pressurized gas storage or diode heat pipe as alternates [25]. The gas gap sorption thermal switch consists of an absorption bed which creates a vacuum environment (less than .001 torr) when it is cooled by absorbing the working gas. When the interstitial fluid is absorbed the switch is transferring no heat and is in the "off" state. The "on" state occurs when the gas is released. Gas gap sorption thermal switch is not passively activated like a bi-metallic thermal switch would be.

Milanez presents a bi-metallic thermal switch for space applications [26]. It has been initially developed to attach cryogenic systems to satellite structures. By using dissimilar metals with different coefficients of thermal expansion the thermal resistance is regulated. The thermal switch is composed of a rod with a thick washer between two nuts. The rod is made of low thermal expansion material while the washers coefficient of thermal expansion is much greater. At room temperature the thermal switch is assembled with a controlled applied torque to the nuts. When the switch becomes cryogenically cooled the washer shrinks and breaks the conduction path with the washers and the two systems become thermally isolating, thus minimizing the heat load coming from the satellite structure to the cryogenic system. The heat switch is passively actuated. The experimental study consisted of measuring the thermal resistance as a function of temperature of a prototype heat switch. Passively activated switches work well for applications where power is not readily available. However thermal switches can also be activated electronically.

An electromechanical thermal switch developed by Beaseley[27] consists of gold membranes with highly emmisive coatings connected to a radiator through SU-8 posts. The switch is electrostatically actuated and when actuated comes in contact with the radiator forming a highly conductive path for heat to escape. Various sizes of the thermal switch have been fabricated and will be tested aboard Midstar 1, a small satellite being designed and built by students at the U.S. Naval Academy. Another form of these electromechanical thermal switches named Active Radiator Tile (ART) has also been developed for orbital satellite heat control applications.

The tiles are micromachined from silicon with anisotropically etched membranes [28]. The interior cavity surfaces would ideally be coated with a low emissivity layers while the exposed exterior surface would be coated with a highly emmisive layer of paint. An array of these microscale devices would be necessary for the suggested use on a macroscale device, the satellite. Surface area on the order of multiple square meters would be required. Problems occurred in the tradeoff between good optical characteristics and desirable electrical characteristics.

Thermal switches provide a way to control heat transfer in and out of devices. Many applications for thermal switches are found aboard space shuttles, satellites, and surveillance mechanisms. Most applications of thermal switch that have been assessed to this point deal with cryogenic applications which means subzero temperatures. The most common types of thermal switches are Gas storage gas gap, sorption gas gap, diode heat pipes, bi-metallic, and microelectromechanical thermal switches.

A mercury micro-droplet thermal switch has been developed by Christenson[3] for use in the P3 heat engine. A single engine produces around a microwatt of power and the need for many engines in series to increase the power output has been realized. The efficiency of the P^3 engine has many factors which are outside the scope of this paper however high power output is related to largest engine cavity strain. Large strain in the engine cavity can only be obtained by cyclic heating and cooling of the engine. Due to the high thermal conductivity of air a gas gap micro thermal switch has been proposed with various interstitial mediums.

1.3 RESEARCH OBJECTIVES

The primary objective of this research was to make thermal resistance measurements of a mercury micro-droplet thermal switch with various gas gaps.

Previously thermal resistance measurements of micro-thermal switches had been conducted only in air [3]. The experiments conducted in this thesis were performed in air at ambient pressure (760 torr), air at low pressure (0.5 torr) and xenon at ambient pressure (760 torr).

To achieve these goals an existing test stand was modified and improved. The test stand was calibrated using a blank Si die in three mediums: ambient air, ambient xenon, and low pressure air. The test stand calibration was conducted to account for heat losses in the test stand. After successful completion of these measurements Si dies with arrays consisting of 1600 droplets were prepared and tested in the same gases. The results of these tests were then used to characterize the micro thermal switch

Chapter 2 MERCURY DEPOSITION

Mercury micro-droplets are used in the micro thermal switch to reduce thermal contact resistance, and decrease wear associated with solid-solid contacts. Physical vapor deposition was used to produce the mercury micro-droplets. Statistical analysis was conducted on each individual dies used in the experiments to account for variations in droplet diameters. Procedures were developed for mercury deposition that provide the necessary results and also provide adequate safety.

2.1 MERCURY DEPOSITION SETUP

Mercury micro-droplet arrays were formed on silicon substrates by means of physical vapor deposition. The deposition chamber was built by Christensen [3] and based on a design by Kim [29]. A schematic of the setup can be seen in Figure 2.1.

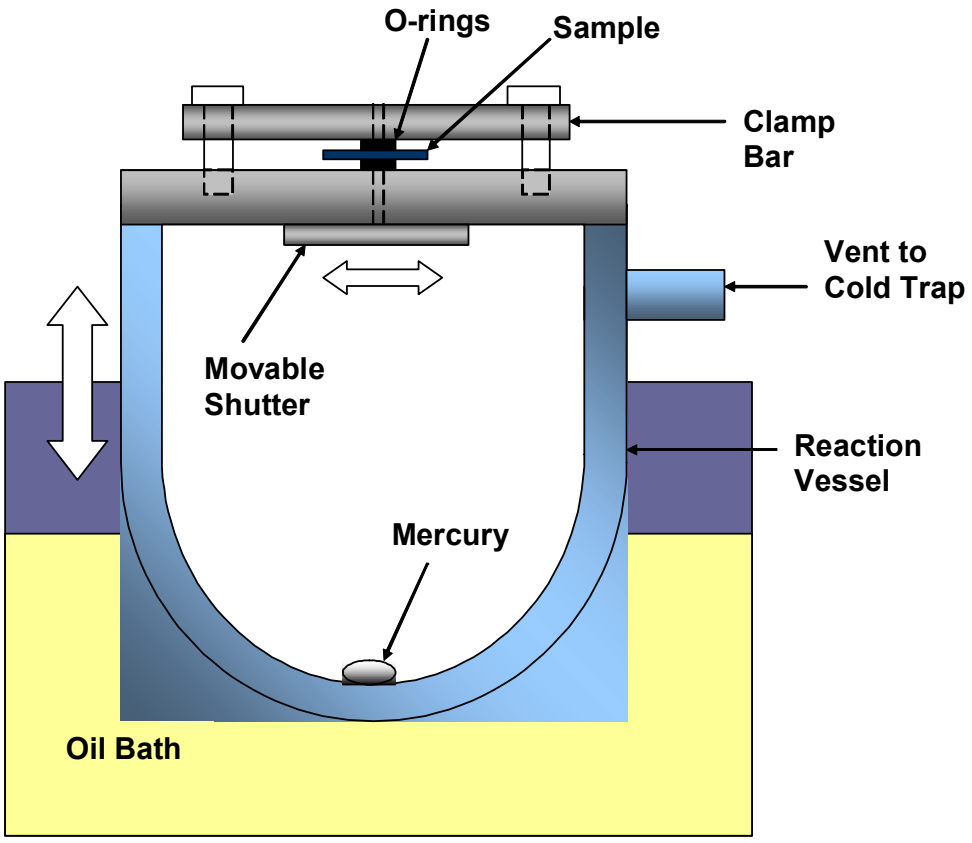

Figure 2.1: Schematic of deposition chamber [3]

A 500 mL glass chamber and PTFE lid, are sealed together with a jar clamp to form a reaction vessel for a small puddle of mercury. The PTFE lid has one small hole to allow mercury vapor to deposit on a die. The clamping bar provides the force used to

seal the o-rings around the die. On the bottom side there is a shutter which opens and closes, controlling access to the through hole in the lid. The vent to the cold trap prevents pressure build up while also preventing mercury vapor from escaping into the atmosphere. The chamber is affixed to a small rod to hold it stationary.

Below the chamber rests a glass beaker filled with mineral oil. This sits on a hot plate which heats the mineral oil bath. A glass thermometer rests in the oil bath to monitor the temperature. The oil bath supplies a constant temperature heat source for the mercury chamber. The heat source rests on an accordion-type stage which allows for vertical displacement.

The deposition apparatus is contained in a fume hood to prevent mercury vapor from escaping. The simple setup consisting of a glass mercury chamber, oil bath, and hot plate provides a very effective way of depositing mercury on silicon samples.

2.2 MERCURY DEPOSITION PROCEDURES

Several improvements have been made to the mercury deposition process since Christensen's experiments [3]. Past deposition included using a resistance heater on the experimental dies to increase the temperature of the die to prevent unwanted deposition. Unfortunately this process resulted in more sporadic droplets than was desirable. Development of unwanted droplets has been reduced by spinning a layer of photoresist on the die and removing the photoresist covering the gold pads. Mercury does not adhere to photoresist.

Dies are made from a (100), 3 inch diameter silicon wafer. First a 100 nm thick silicon dioxide layer is grown using a wet oxidation process. Photolithography is performed to pattern the Pt. A thickness of 175 nm of platinum is sputtered on one side

of the die. The unwanted platinum is removed, using a "lift off" technique. This procedure produces a thin film platinum RTD (Resistance Temperature Detector) and a resistance heater, which can be seen in Figure 2.2. A more detailed discussion of these devices can be found in Chapter 3.

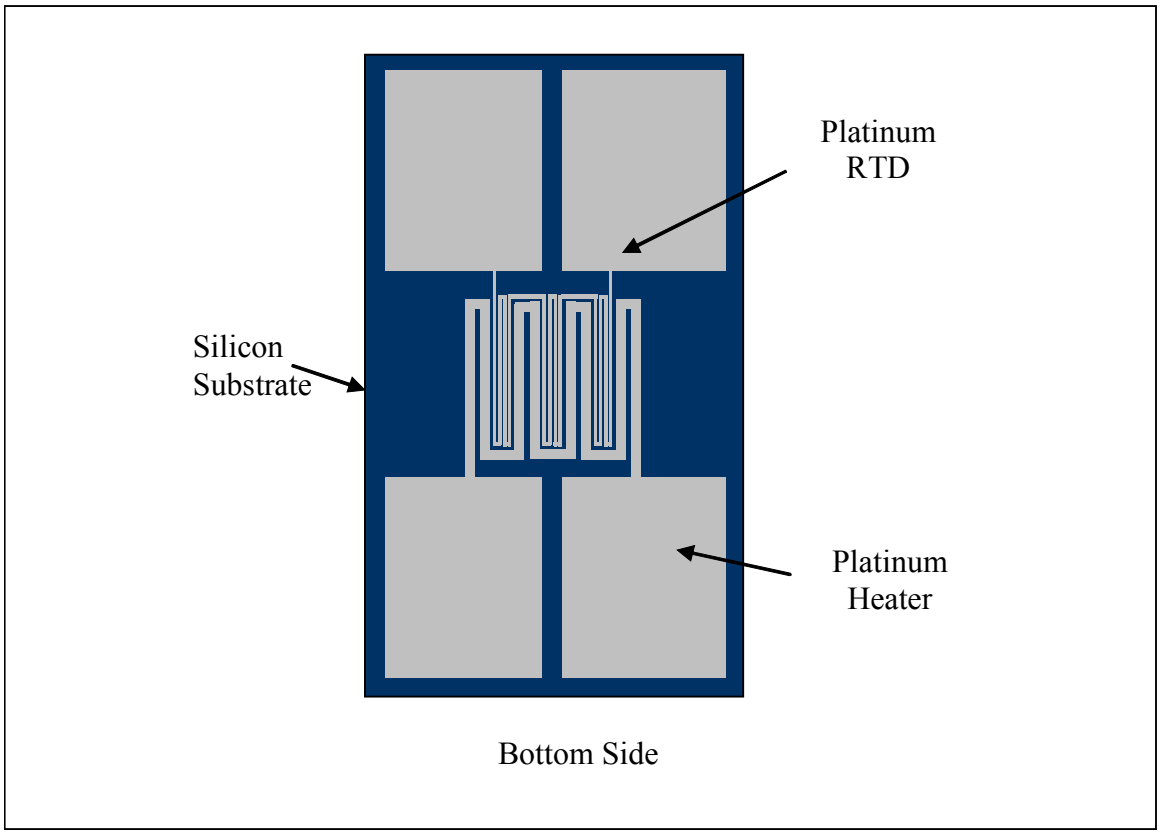

Figure 2.2: Depiction of platinum resistance heater and RTD

The other side of the die is sputtered with a 5 nm adhesion layer of titanium/tungsten followed by a 300 nm layer of gold. The platinum and gold are applied using DC sputtering in a chamber pressure of 7.5 mTorr. The titanium/tungsten is sputtered at 100W while the gold is sputtered at 75 W. Photolithography and gold etching after gold deposition are performed which results in 22 arrays of 1600 gold pads per wafer. A schematic of one array can be seen in Figure 2.3.

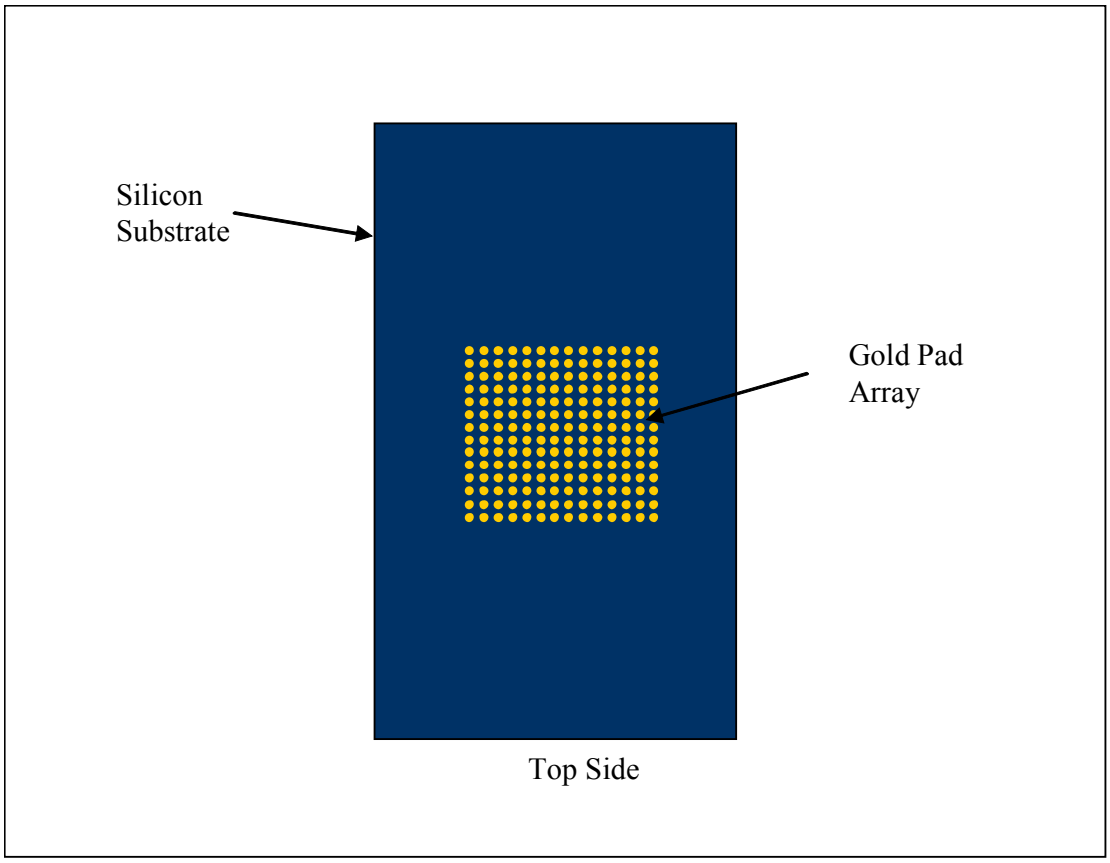

Figure 2.3: Depiction of processed gold pad array.

Once dies have been prepared with gold pad arrays, a thin layer of photoresist is spun onto the gold side. A negative array mask is then applied and exposed to UV light. The photoresist is then developed in AZ400K developer. The photoresist is removed from the gold pads.

The die with photoresist is rinsed under deionized water for 2 minutes and is dried with canned air. Next the die is taken to the deposition chamber. The clamping bar is removed as well as the top o-ring and glass slide. The glass slide is placed between the o-ring seals when no deposition is taking place to prevent mercury vapor from leaving the chamber. To prevent contamination, both o-rings are cleaned with isopropanol. The die

is placed over the small hole in the lid of the mercury chamber. The gold pads are placed face down, exposing them to the mercury vapor below. Care must be taken when putting die in the chamber. Misalignment can result in uneven or no deposition. The top o-ring is replaced and the die gets sandwiched in the apparatus using the clamping bar as shown in Figure 2.1.

Before cleaning the die the hot plate is turned on to bring the oil bath to a temperature of 100^{o} C. At this temperature the oil does not vaporize, and contaminate the die. Heating up the oil bath early decreases the time required for the full deposition process. Once the die has been placed in the chamber the hot plate is turned up so the oil bath reaches a temperature between 170-180^{o}C. The oil bath is raised to partially submerse the mercury chamber. The glass chamber is positioned so that it does not rest on the bottom of the oil bath container. If the oil does not meet the minimum depth for an accurate thermometer reading then additional mineral oil is added.

The chamber is allowed to heat up for 30 minutes, after which the shutter is opened exposing the die to mercury vapor. The die is exposed to mercury vapor for one hour and then the shutter is closed. Next the hotplate is turned off and the oil bath is lowered until the chamber no longer contacts the oil. After the chamber has cooled for 15 minutes the clamping bar and mercury die are removed. While handling the dies after deposition care is taken to prevent smearing the micro-droplets.

The glass slide and top o-ring are replaced and the o-rings clamped down with the aluminum bar to prevent mercury vapor leakage.

2.3 DROPLET STATISTICAL ANALYSIS

The work used in the subsequent experiments was conducted by K.Crain [30]. The three mercury droplet arrays used in the present work were characterized to determine the distribution of mercury droplet diameters. Eight photographs were taken across both diagonals for each of the experimental dies. One picture was also taken of a scale which was used in conjunction with Scion Image software to measure the droplet diameters. Histograms of droplet diameters were produced and average droplet diameter and standard deviations were calculated.

The histogram of the experimental dies used in the mercury micro-droplet experiment in air at ambient pressure is given in Figure 2.4. The sample population was 269 droplets and the average droplet diameter was 26.41μm with a standard deviation of 4.35μm.

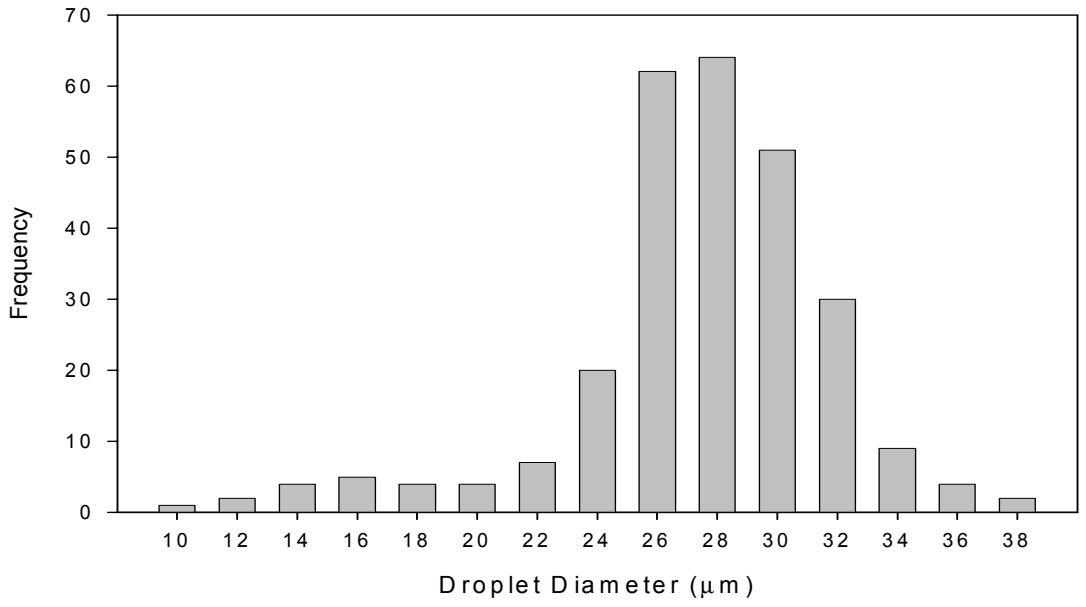

Figure 2.4: Histogram of droplets for die used in 760 torr air experiment.

For the mercury micro droplet experiment in air at 0.5 torr a sample size of 246 droplets was characterized. The mean diameter of droplets in this array was 32.08 μm with a standard deviation of 7.31 μm. A frequency histogram of the mercury droplet array characterization can be seen in Figure 2.5.

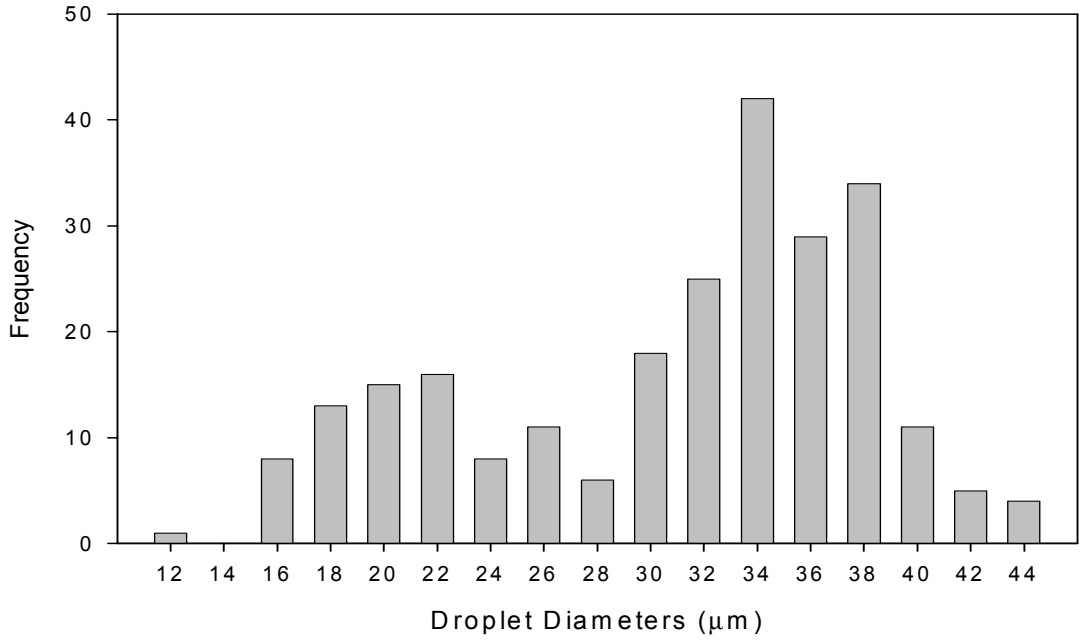

Figure 2.5: Histogram of droplets for die used in 0.5 torr air experiment.

The final mercury micro droplet array used was for the micro-droplet experiment conducted in xenon at 760 torr. The droplet diameters were characterized using a population of 278 droplets. The mean diameter was 29.52 μm. The standard deviation of the droplet diameters was 4.90 μm. A histogram of the frequency distribution is presented in Figure 2.6.

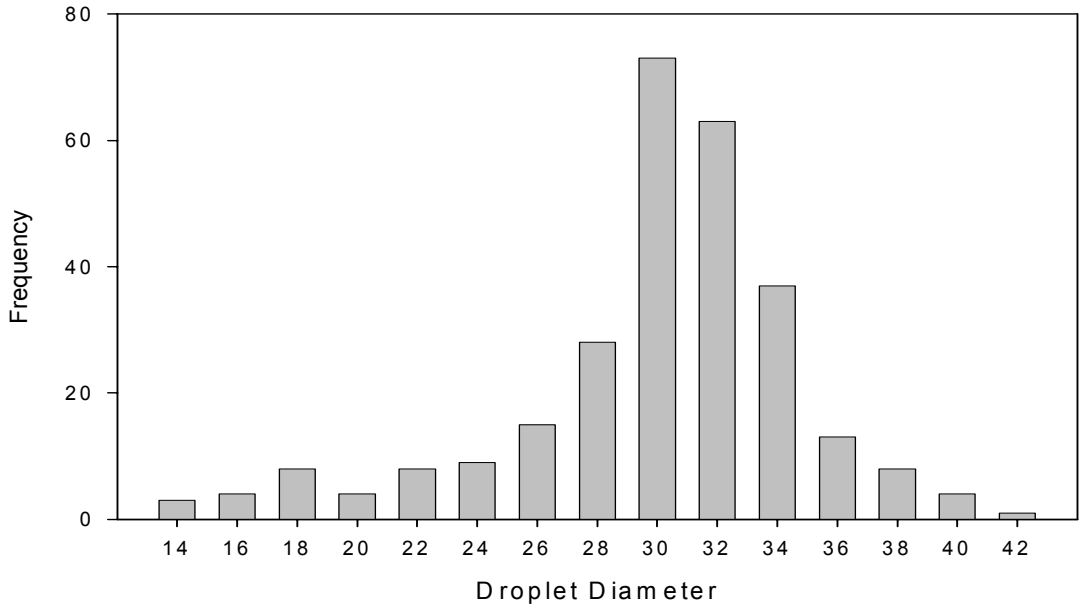

Figure 2.6: Histogram of droplets used in 760 torr xenon experiment.

The statistical analysis shows that the mean diameter of the three dies used in the mercury micro droplet arrays ranged from 26.41-32.08 μm.

2.4 MERCURY SAFETY

Mercury deposition conducted at Washington State University is safely conducted in a fume hood. The fume hood vents any mercury vapor that might be released during deposition. Conducting heat transfer measurements with a mercury array die can not be done practically in a fume hood, calculations by Christensen [3] indicated that safe use of the mercury micro-droplet arrays does not require a fume hood. If all 1600 mercury droplets, with a diameter of roughly 30 μm, were to evaporate in the lab the concentration would be two orders of magnitude less than that required by OSHA [31]. Gloves are worn when dealing with mercury for deposition and experimentation. Even though

mercury is a poisonous metal that can have adverse affects depending on duration of exposure and concentrations, the minimal amount used in the experiments presented in this thesis does not pose a physical threat.

Chapter 3 STEADY STATE HEAT TRANSFER

3.1 DIE PREPARATION

Standard micromachining techniques were used to fabricate all experimental dies used in the experiments presented here. Sputtering, photolithography, annealing and etching are the processes used in die preparation.

Two dies are used in each experiment. One die, the Heater or Top Die has a platinum RTD/Heater on one side and is blank on the other. The second die, the Droplet or Bottom Die, has platinum RTD/Heater on one side and gold targets on the other. Both dies are approximately 10 mm X 18 mm rectangles diced from 3 inch silicon wafers. Twenty two dies can be fabricated from one 3 inch silicon wafer.

The fabrication steps for gold target preparation were outlined in Chapter 2. The detailed processing of the platinum heaters and RTD are now discussed. Immediately following oxidization of the silicon die, photolithography is performed on the side of the wafer to be sputtered with platinum. The mask of the desired pattern can be seen in Figure 3.1. A detailed drawing of the heater/RTD can be seen in Figure 2.2.

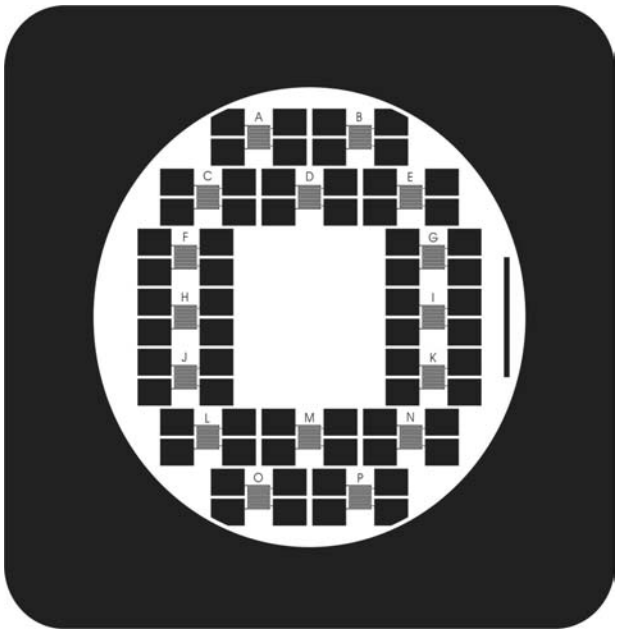

Figure 3.1: Negative mask of platinum RTD/heater.

Photoresist, AZ5214, is spun onto the wafer and exposed to ultraviolet light. Once the photoresist is exposed and developed a 170 nm layer of platinum is sputtered. After the platinum has been sputtered the wafer is soaked in acetone, which dissolves the photoresist, and the Pt is removed in a "lift off" process. Finally the wafer is annealed at 700^{o}C for 10 minutes completing the processing of the platinum RTD/Heater. Details of this procedure can be found in Cho [32].

After completion of the platinum RTD/Heater the gold targets are fabricated using the techniques described in Chapter 2. The mask used can be seen in Figure 3.2. A detailed drawing of the gold target array can be seen in Figure 2.3.

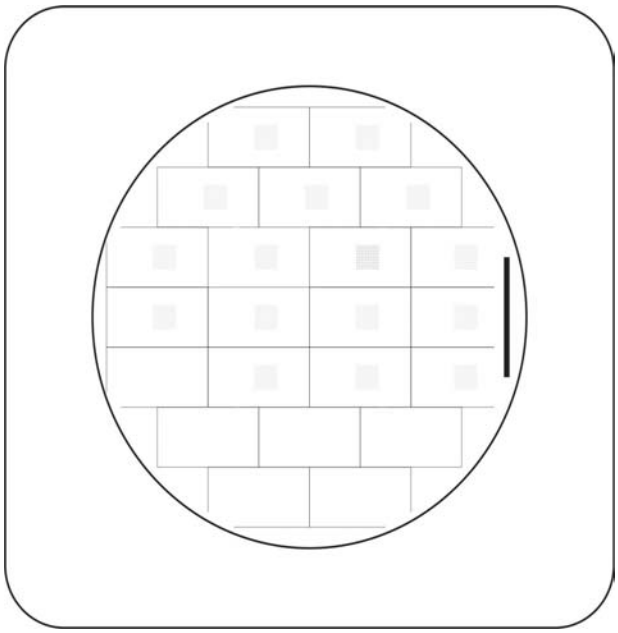

Figure 3.2: Mask for gold processing, 1600 pad and blank dies.

Of the 22 dies on a 3 inch wafer, 16 are fabricated with 30 micron diameter gold targets and the remaining 6 are left blank. Only one wafer is required for completion of these experiments.

3.2 EXPERIMENTAL SETUP

3.2.1 Test Stand

The test stand consists of four stainless steel legs mounted on a vacuum bell jar base plate. An aluminum carrier is bolted to the top of the test stand legs. The carrier supports a guard-heated calorimeter and experimental dies. Centered in the space between the four test stand legs is a linear stage with an X-Z bracket for vertical

displacement. A heat sink is affixed to the top of the stage. A photograph of the test stand can be seen in Figure 3.3.

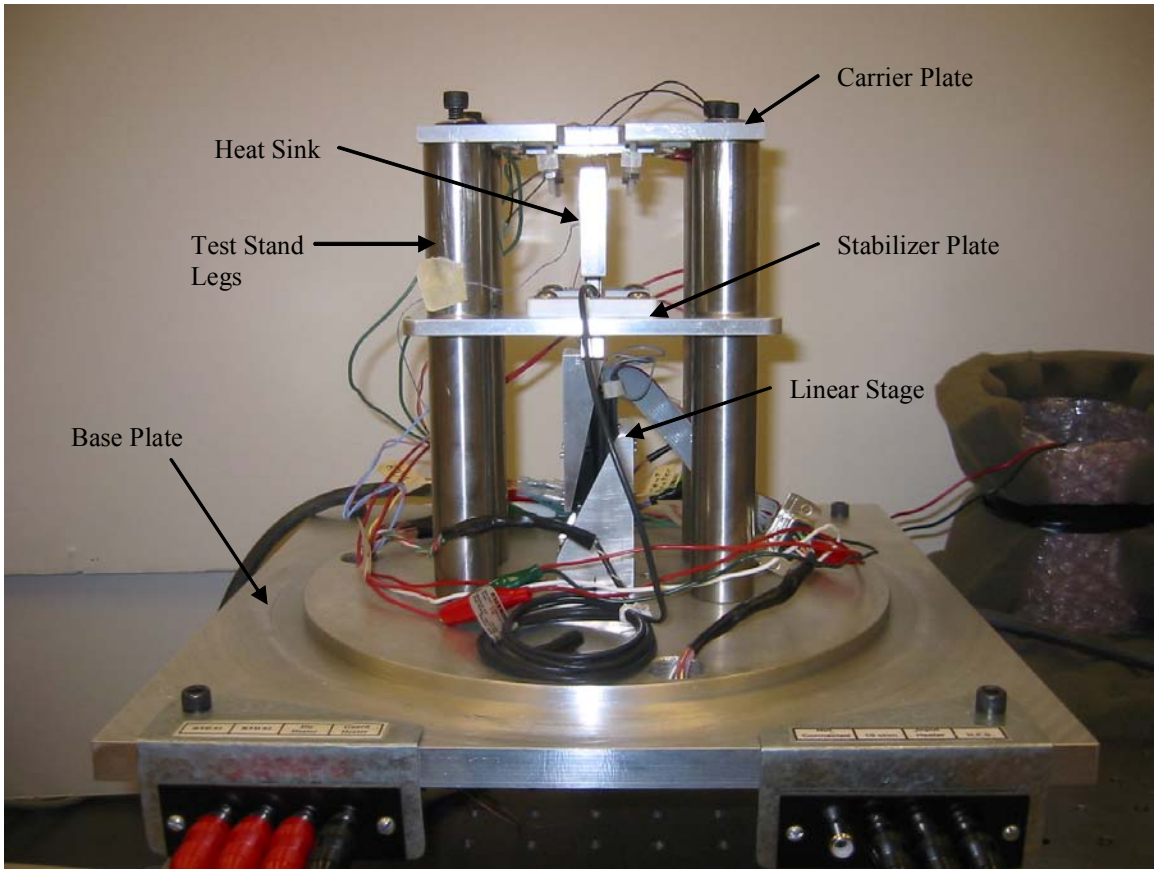

Figure 3.3: Photograph of experimental test stand with labels.

The aluminum carrier plate supports a guard heater, heat flux sensor, circuit board, and an experimental die. Figure 3.4 is a schematic of the carrier plate stack.

Two 5 cm X 5 cm kapton insulated flexible resistance heaters are attached to the top of the aluminum carrier plate with pressure sensitive adhesive. The heaters are wired in series with a maximum power rating of 10 W at 28 V. The guard heater acts as an active insulator. To make a measurement, the heat flux sensor is zeroed by adjusting the

power delivered to the guard heater. When the heat flux sensor is zeroed all the input heat is assumed to be traveling down through the micro-droplet array and thermal switch.

Directly on the bottom of the carrier plate, a small aluminum spacer is mounted with the same dimensions as the heat flux sensor. The heat flux sensor is sandwiched between the top aluminum spacer and another stiffening aluminum plate measuring 20 mm X 50 mm. The heat flux sensor is a 40 junction thin-film thermopile measuring 20 mm X 25 mm, which is mounted in kapton. It has a resolution of 20 mV/(W/cm^2).

The bottom aluminum plate acts as a stiffener for the circuit board that the top die is mounted to. The circuit board has four copper electrodes that allow the die RTD and heater to connect electrically with copper pads mounted to the carrier plate. The top die is glued to the circuit board with an electrically conductive two part epoxy, Aremco 556. The purpose of the circuit board is to prevent the heater/RTD from contacting the mercury micro-droplets during experiments. The carrier plate and stack are shown schematically in Figure 3.4.

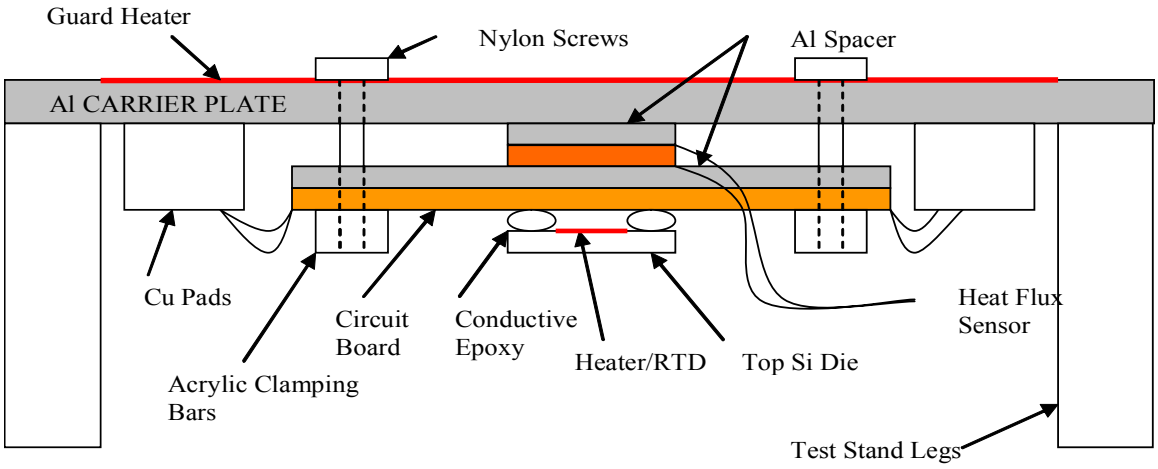

Figure 3.4: Carrier plate and stack schematic.

A thin circuit board was used to make the electrodes for the connection to the heater and RTD's on the top die. Standard photolithographie techniques were used to pattern the circuit board. A mask was made using clear plastic and four strips of tape approximately 2 mm wide. Copper etchant (Ferric Chloride) was used to etch away unwanted copper.

The stack is securely fastened to the top carrier plate with acrylic clamping bars and nylon screws. Connections to the heater and RTD are made using fine wire bonded to the copper circuit board. The fine wire helps to thermally isolate the top die.

The bottom die is attached to the heat sink with kapton tape. It rests against another silicon die used for alignment. Aligning the dies is crucial for making accurate thermal resistance measurements at small gap lengths. The alignment die, diced from a single-side polished 3 inch wafer, is attached to the heat sink with Aremco 556. The use of a highly viscous epoxy enables the alignment die to conform to the angle of the top die when setting up the apparatus for testing. To set the alignment die, a ~2 mm droplet of epoxy is placed on the heat sink and the alignment wafer is positioned on top of the droplet. The alignment die is then brought into contact with the top die and pressure is applied to make the dies parallel. Once the epoxy is cured, the top die and alignment dies are assumed to be parallel.

The heat sink is constructed from a 64 mm X 64 mm X 10 mm aluminum plate. A hole measuring 32 mm X 32 mm is machined from the center of the carrier to allow for electrical connections to the RTD on the bottom die. A connection is made to the RTD on the bottom die via copper probes glued to an acrylic carrier. A magnet on the carrier and a magnet glued onto the heat sink, as depicted in Figure 3.5, hold the probes in place.

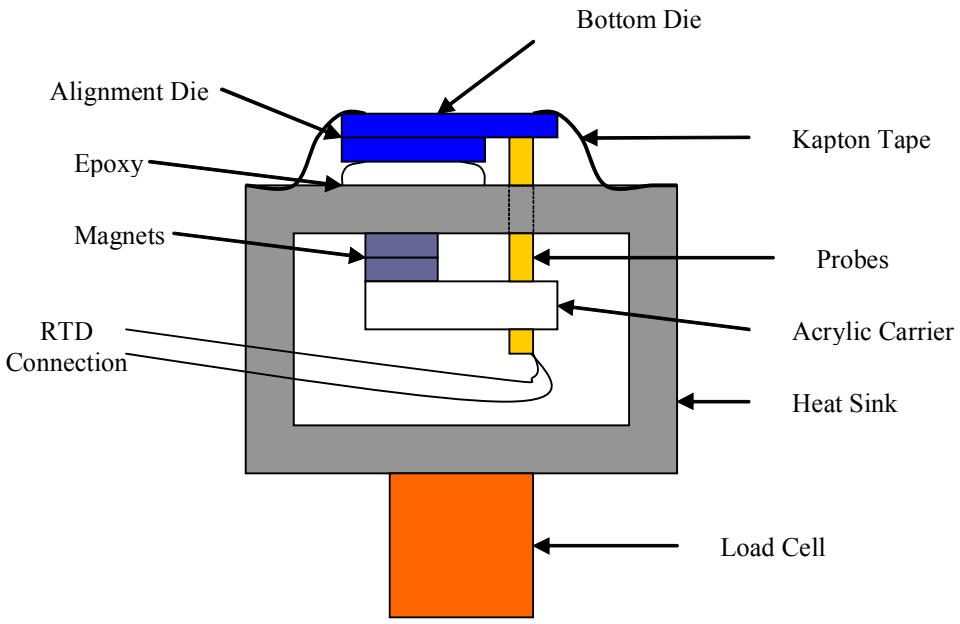

Figure 3.5: Bottom die RTD connection with probes.

The heat sink is mounted to a Futek model L2357, S-Beam Junior load cell with a #4-40 UNC screw. The "S" type load cell was chosen for this application because as a load is applied, the top and bottom surfaces remain parallel. Cantilever type load cells do not have this quality. These two load cell types and their corresponding deflections are depicted in Figure 3.6.

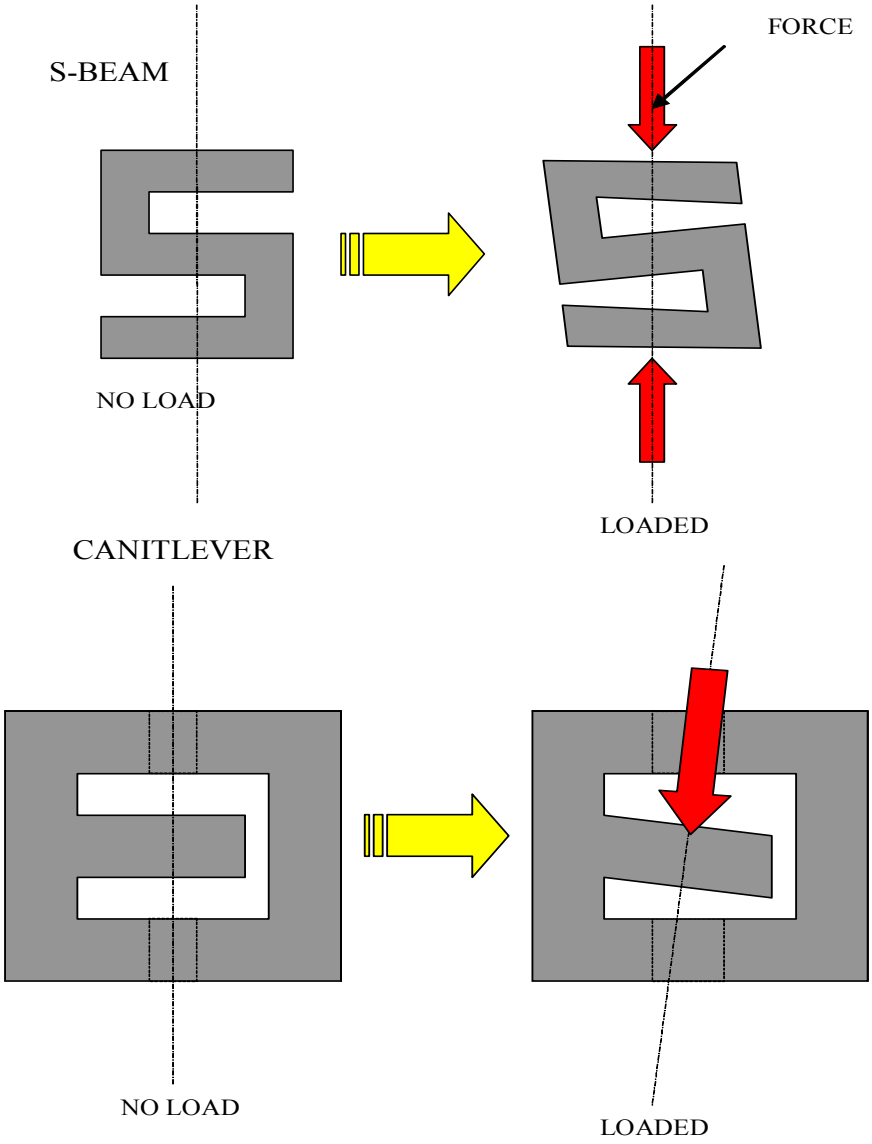

Figure 3.6: Exaggerated depiction of S-beam vs. cantilever type load cell.

The load cell is attached to a stabilizer bar (#4-40 UNC screw) to provide lateral stability. The stabilizer bar is attached to the z-axis stage with a customized adapter plate. The adapter plate attaches the load cell vertically and centers the load on the axis of the linear stage. Guide pins pressed into the adapter plate precisely control the position of

the guide bar. Figure 3.7 shows these test stand features.

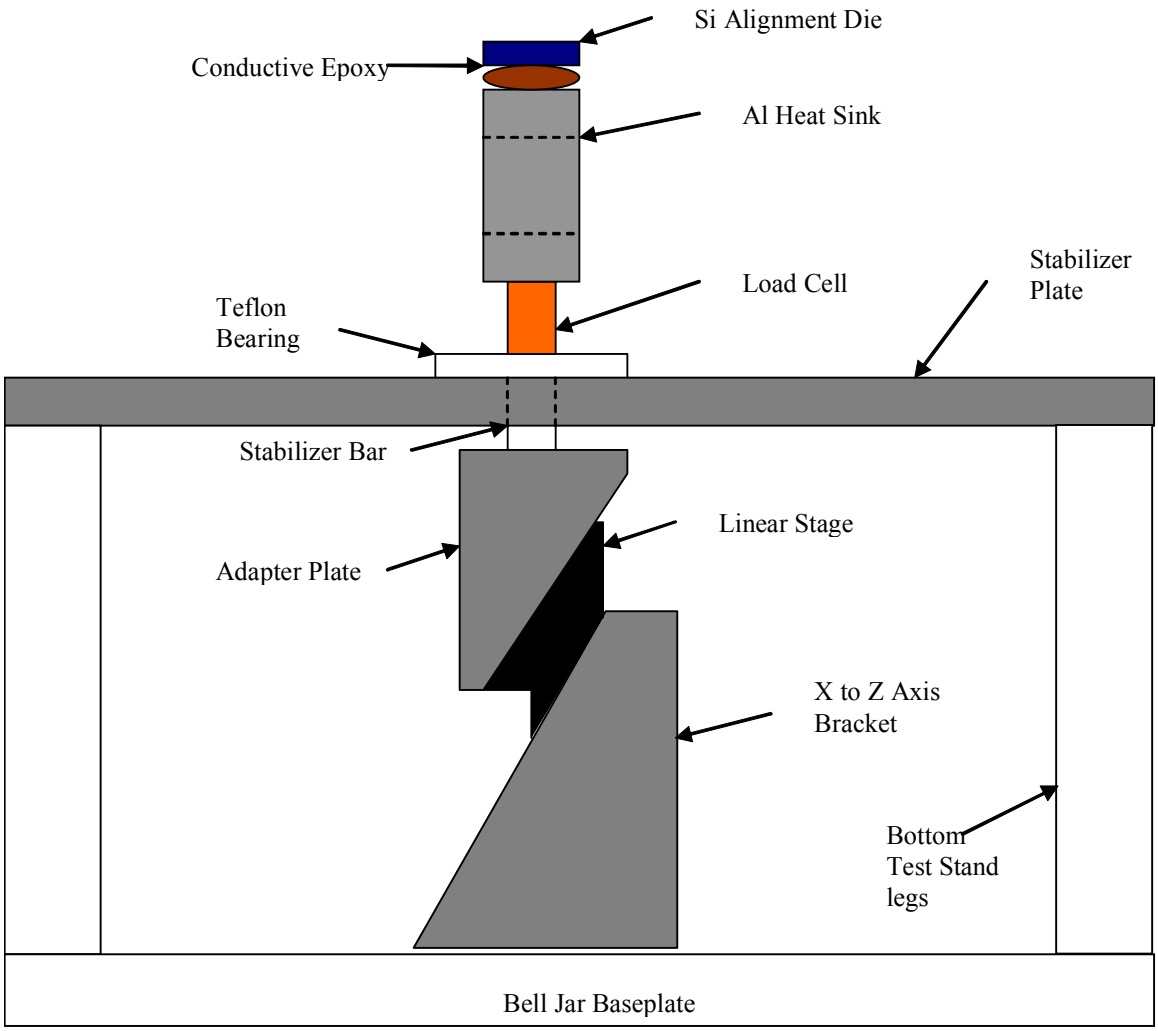

Figure 3.7: Schematic of bottom portion of test stand apparatus.

The guide bar slides on Teflon™ sleeves which are solidly affixed to a stabilizer plate. Sleeves were fabricated to provide a low coefficient of friction surface for the stabilizer bar to slide on. The stabilizer plate fits snugly between the upper and lower portion of the stainless steel test stand legs.

A folded motorized MicroMini™ stage is used to provide control of vertical displacement during experimentation. The MicroMini™ travels up to 25.4mm with a repeatability of ± 2 microns in the standard slider. The capacity is 0.5 kg for direct top or side loading. The linear stage was converted to a z-axis stage with a X-Z bracket fabricated from aluminum. The X-Z bracket orientated the linear stage in a vertical position and is depicted in Figure 3.7. The bottom of the X-Z bracket is attached to the bell jar base-plate with two ¼-20 screws.

The base-plate consists of a 30.5 cm^2 piece of aluminum. A raised circular section in the center of the plate is used for bell jar alignment. The gasket-aluminum interface area is sanded smooth to ensure a leak free seal. Two NPT PAVE-Seals were purchased from Pave Technology Co. for electrical connections passing through the aluminum base-plate. Seals were leak tested by the manufacturer at 550 kPa for 1 minute. A ¼" NPT Swagelok™ fitting is used for the vacuum connection to the base-plate. Teflon tape is used on all threaded attachments to the base-plate. The Swagelok™ fitting is connected to a manifold of valves and fittings which allows for vacuum applications and for filling the bell jar with a gas.

The vacuum bell jar used is a 10"X12" Pyrex™, manufactured by Corning. A 10" L gasket is used for sealing between the base-plate and bell jar. Corning vacuum grease is spread on the L gasket to provide a non-leaking interface. A 10" metal guard provides needed safety should the bell jar implode.

3.2.2 Instrumentation

Figure 3.8 illustrates the instrumentation required this experiment.

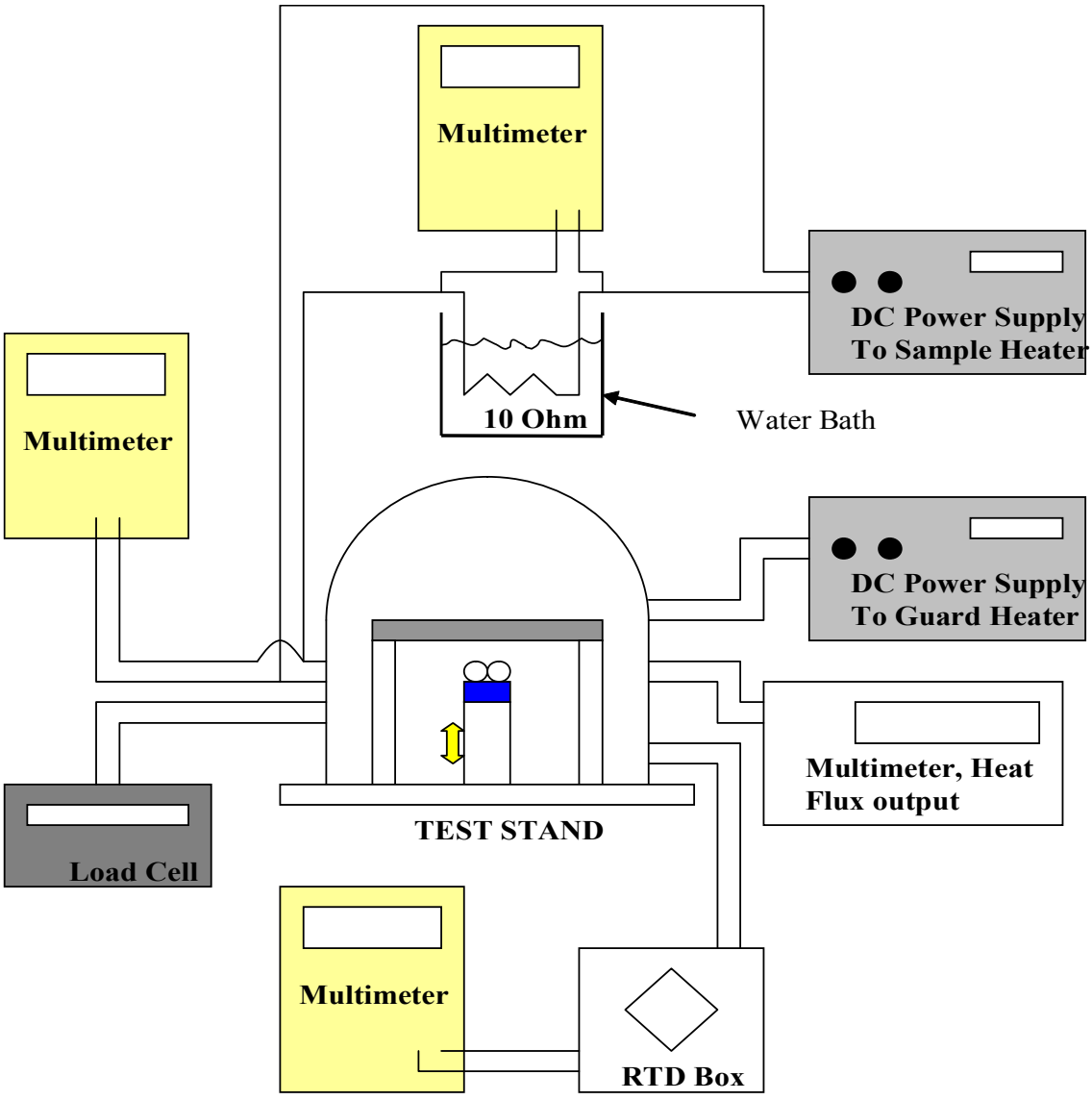

Figure 3.8: Diagram of electronic component connections for experimental setup.

A Hewlett Packard model E-3610A (0-15 V DC) power supply is used to deliver power to the input heater die. A 10 Ω resistor wired in series with the input heater is used to measure the current through the heater. The resistor is held in a bath of deionized water to keep the resistor at a constant temperature during the experiments. The voltage drop across the 10 Ω resistor and input heater are measured using handheld Fluke, model

189, multimeters with +/- 0.5 mV resolution. Three identical multimeters are used in these experiments.

The guard heater, which provides active insulation to the apparatus, is powered by a 0-15V DC power supply. A heat flux sensor is used to minimize heat losses out the back of the guard-heated calorimeter. The heat flux sensor is model HFS-4 manufactured by Omega with a nominal resistance of 175Ω at room temperature. The conversion between output voltage and heat flux is 20 (mV-cm^2/W). The heat flux sensor is monitored with a Hewlett Packard model 34401A multimeter with a resolution of ±0.0005mV.

The temperature differential across the thermal switch is obtained using two RTD's with a Wheatstone bridge circuit and amplifier. The Wheatstone bridge circuit and amplifier are depicted in Figure 3.9. Through RTD calibrations the voltage output from the bridge circuit is related to the temperature differential across the thermal switch.

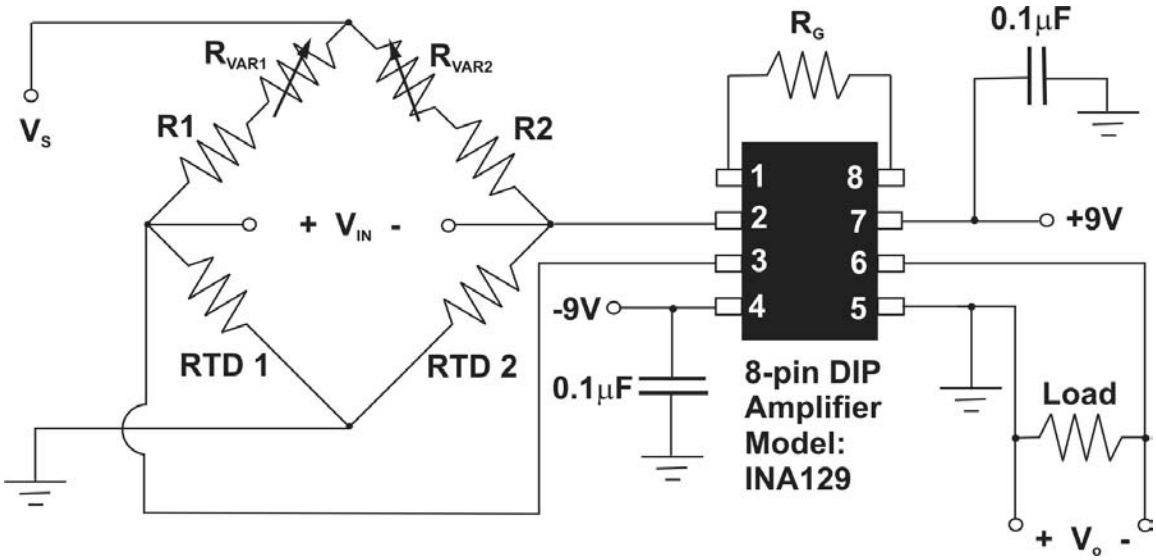

Figure 3.9: Circuit diagram for differential temperature measurements [3]

The circuit diagram for differential temperature measurements is shown in Figure 3.9. The voltage source (V_s) used for the wheatstone bridge circuit is one 1.5V size C alkaline battery. RTD1 and RTD 2 are the top and bottom dies respectively. R1 and R2 are constant 3.3 kΩ resistors. The variable resistors (R_{var1} and R_{var2}) are rheostats with an adjustable resistance from 0-25 Ω.

The amplifier multiplies the output voltage from the Wheatstone bridge circuit by 500 times to provide a voltage output that is detectable using a multimeter. Due to the amplification it is necessary to reduce noise in the signal. This is accomplished through the use of two 0.1μF capacitors shown in Figure 3.9. The ±9 V source connected to the amplifier is provided with 9 V batteries.

The motorized linear stage is controlled with a MicroMini™ (model 2000) controller. The step size can be programmed for desired units of measure. In the present set of experiments the step size was set to 0.5 μm.

The applied force is measured and recorded using a load cell and digital readout produced by Futek. The digital readout is model IPM500 and was calibrated 8/27/04. Calibrations are good for 1 year) by Futek. The load cell is a LSB200 Jr. S-Beam type.

To perform experiments in controlled gas environments, such as vacuum and xenon gas, additional instrumentation is required. A manifold consisting of shutoff valves, gauges and copper tubing is connected to the bottom of the bell jar base-plate with a ¼" NPT Swagelok fitting. A copper tee fitting immediately following the connection to the base-plate is used to fill the bell jar with xenon. Figure 3.10 shows schematically the connections of the manifold.

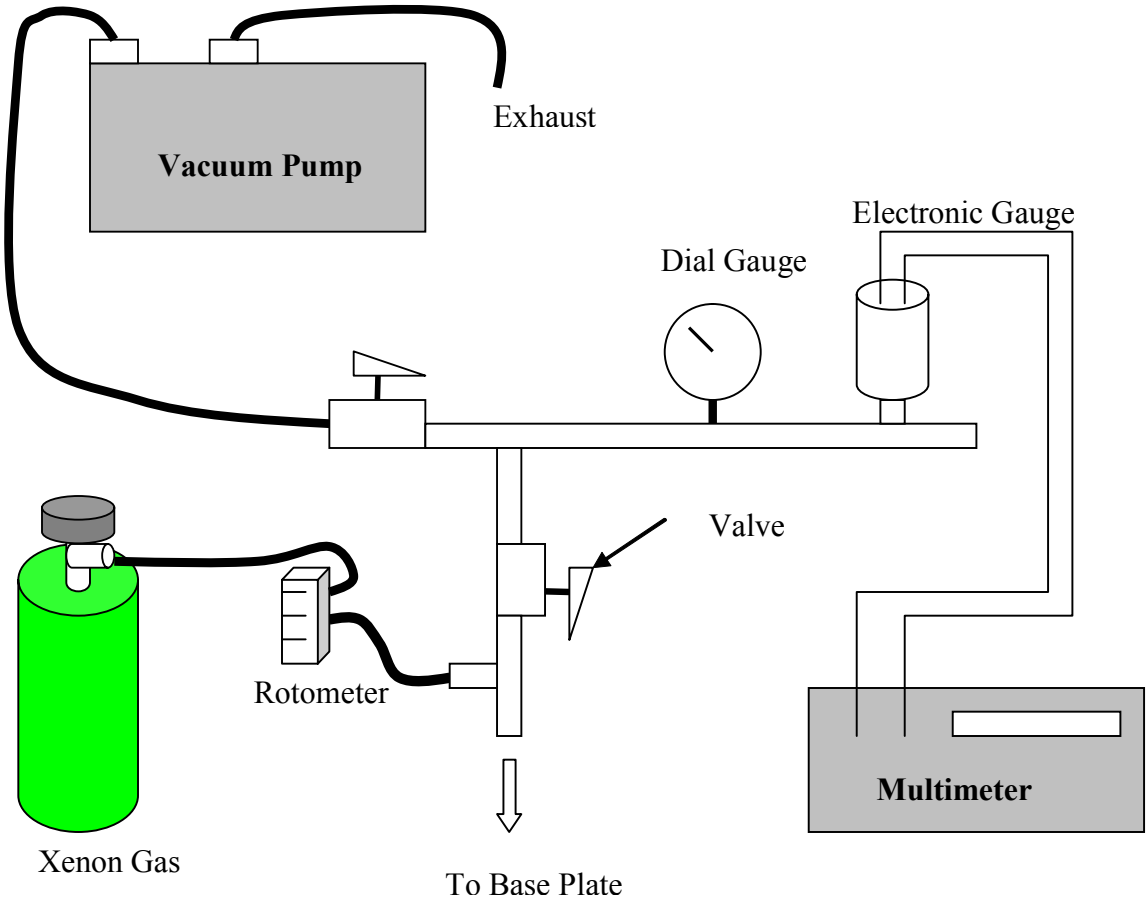

Figure 3.10: Manifold diagram for vacuum and xenon experiments.

Due to leaks in the manifold a constant flow of gas is delivered to the bell jar during xenon gas experiments. A Dwyer rotometer with a resolution of 0.05 Lpm is used to gauge the flow of xenon to the bell jar.

During the low pressure air experiments the dial gauge and electronic gauge are both used to monitor the pressure. The dial gauge is an Ashcroft with a resolution of 0.5 in-Hg down to 28 in-Hg vacuum or 660 torr. The low pressure electronic gauge does not

read accurately above 10 torr. The electronic gauge is a MKS model 722A11TGA2FL with an accuracy of 0.5% of 1 torr. An HP multimeter is used to measure the voltage from the electronic gauge. One volt gauge equals 1 torr. Bell jar pressure is regulated with the valve closest to the vacuum pump in Figure 3.10. The vacuum pump used for these experiments is a Welch w-series model T55JXCFH-1280. The pressure used in these experiments, 0.5 torr, is obtained within ~3 minutes of pump operation.

3.3 EXPERIMENTAL PROCEDURES

3.3.1 RTD Calibration

The relationship between the voltage output of the Wheatstone bridge circuit and the temperature differential is determined with an RTD calibration. One experimental top die is used throughout the heat transfer experiments. The primary reason to use one top die is that the top die is aligned with the alignment die (discussed in the next section), Changing top dies during experimentation would require realignment which is a time consuming procedure. Another reason to use only one top die is that the top die is glued to the copper circuit board and clamped onto the top carrier. The experimental procedure is simplified by using only one top die throughout. For this reason prior to calibration all dies which will be used for experimentation are calibrated against the one top die.

Each calibration consists of one top die and one bottom die. The dies to be calibrated are loaded into acrylic carriers and the RTD's are contacted using probes. Once a good connection is verified both acrylic carriers are placed in a constant temperature bath filled with deionized water at ~21^{o}C (room temperature). A foam insulated cup is used to prevent sudden temperature changes. Once the dies have reached

steady state in the constant temperature bath the RTD bridge circuit is set to zero using the variable rheostats.

After zeroing of the RTD circuit, the top die is placed in an adjacent glass beaker resting on a hot plate. The initial temperature of the bath is close to room temperature. A stir bar is used to maintain a uniform temperature while the beaker is heated. Once the die is placed in the heated bath the hot plate and stir bar are turned on.

Both the voltage output from the amplified Wheatstone bridge circuit and a liquid-in-glass thermometer are monitored. The glass thermometer has a resolution of 0.5°C. A calibration curve is constructed from the measured temperature difference between the two baths and the corresponding voltage output from the RTD circuit. The differential temperature is obtained by subtracting the measured temperatures of the two water baths. The four calibration curves can be seen in Figures 3.11 through 3.14.

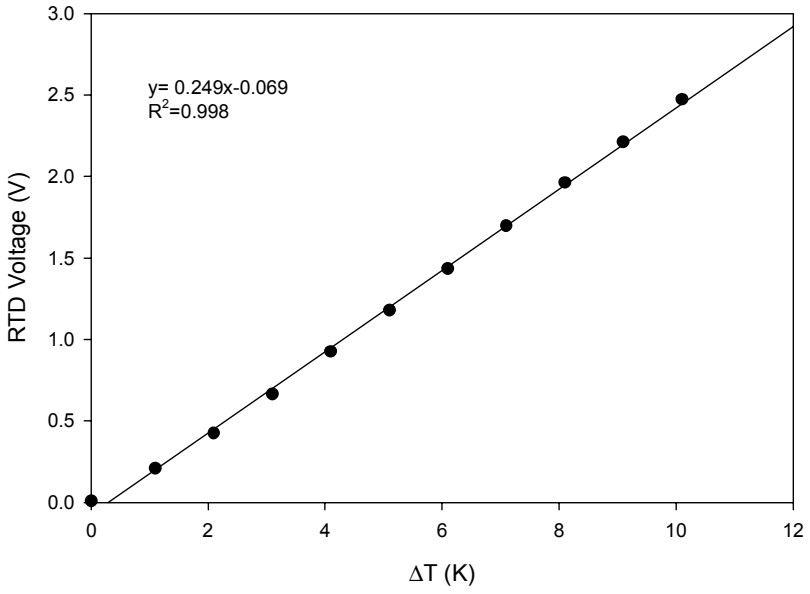

Figure 3.11: RTD calibration for dies used in test stand calibrations.

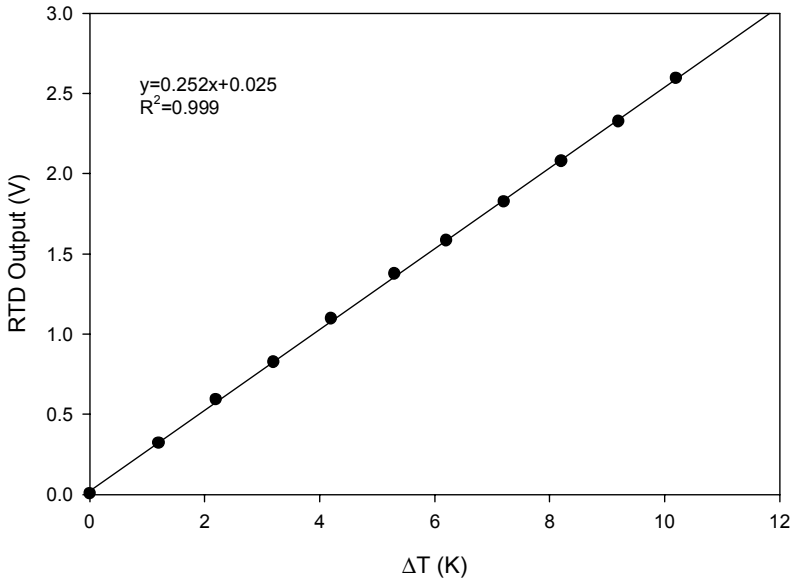

Figure 3.12: RTD calibration for dies used in air at ambient pressure.

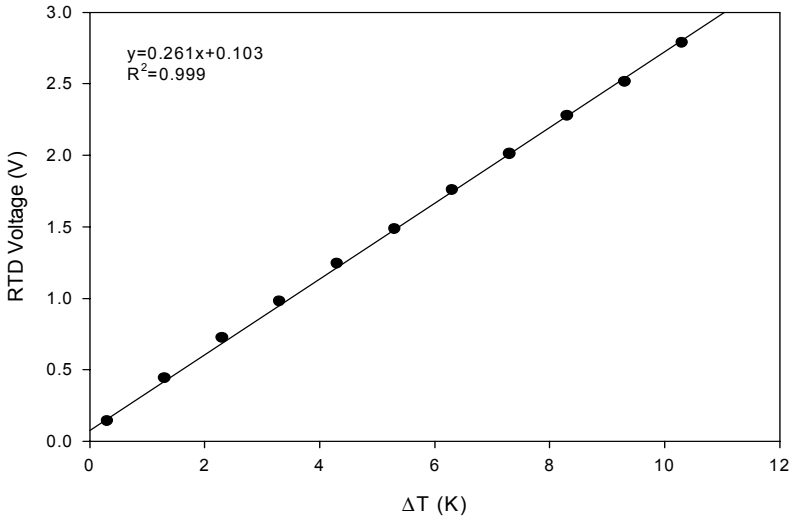

Figure 3.13: RTD calibration for dies used in xenon at ambient pressure.

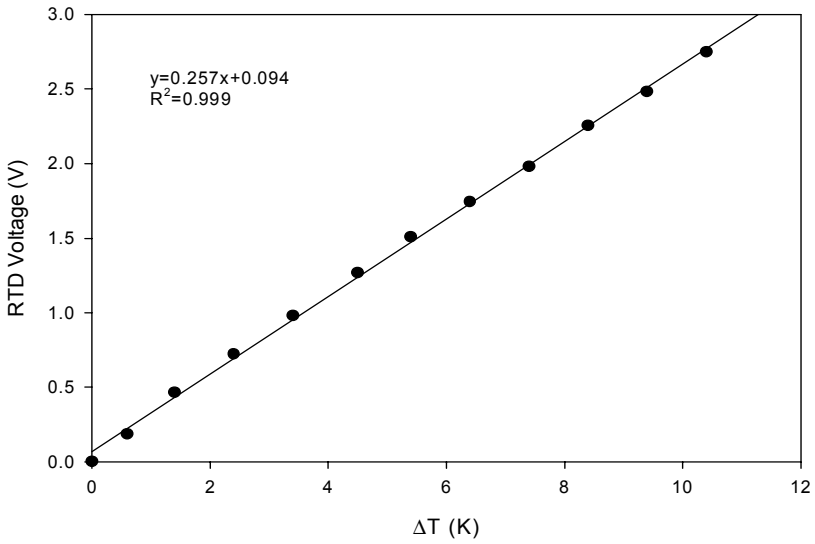

Figure 3.14: RTD calibration for dies used in air at 0.5 torr pressure.

Four bottom dies are calibrated against one top die. One of these four dies, without gold targets, is used for test stand calibrations. Three other dies with gold pads, for mercury deposition, are calibrated for the remaining three sets of experiments.

3.3.2 Test Stand Calibration

Due to heat losses from the test stand calibration is required. A test stand calibration is conducted to quantify the heat losses and to obtain an accurate thermal resistance measurement. The heat loss is accounted for by defining a parallel thermal resistance, or heat path. Heat transfer measurements can then be corrected with the quantified parallel resistance from each test stand calibration.

The thermal conductivity of air and xenon is well documented [4,33]. The thermal conductivities of xenon and air at ambient pressure are 0.00569W/m•K and 0.0263

W/(m•K) respectively. The heat transfer across varying gas gaps can be quantified with the following equation.

$$R_c = \frac{L}{k \bullet A} \tag{3.1}$$

where: R_c is the thermal resistance of the gas gap. (K/W)

L is the length of the gap. (μm)

k is the thermal conductivity of the gas.(W/m•K)

A is the cross sectional area. (m^2)

By comparing the predicted gas gap resistance with the measured thermal resistance the heat losses from the test stand can be determined and quantified as a parallel resistance. To do this the thermal resistance of varying thickness gas gaps are determined. The process begins by aligning the top and bottom dies. Once the dies have been aligned, the bottom die is securely fastened on top of the alignment die using Kapton tape. The dies are brought together using the motorized stage and the alignment is checked visually. Once the alignment is visually verified, the dies are brought into contact and a small load is applied. The heat flux sensor is zeroed at ±0.004 mV. When the heat flux sensor is zero, the Wheatstone bridge circuit is set to zero with the variable resistors.

Next, the guard heater is turned on to an initial setting of 10 V and the apparatus heats up for 15 minutes, the estimated time constant for the guard heater[3]. Voltage is applied to the top die input heater until the heat flux sensor output is zero. When zero, the distance, output voltage of the RTD Wheatstone bridge circuit, voltage drops across the 10 Ω resistor and input heater are recorded

The current in the input heater circuit is calculated with Ohm's law using the voltage drop across the 10 Ω resistor. The power is calculated using that constant circuit current and the voltage drop across the input heater. The calculation is shown below.

$$I = \frac{V_{10}}{R_{10}} \tag{3.2}$$

where: I is the current in the input heater circuit. (Amp)

V_{10} is the measured voltage drop across the 10 ohm resistor.(V)

R_{10} is the value of the electrical resistance of the resistor in the water bath. (Ω)

$$P_{in} = V_H \bullet I \tag{3.3}$$

where: P_{in} is the input power supplied to the top die. (W)

V_H is the measured voltage drop across the input heater.

The RTD calibration of the corresponding dies used in the experiment is used to convert measured voltage output to temperature. The thermal resistance is then calculated by

$$R_m = \frac{\Delta T}{q_{in}} \tag{3.4}$$

where: R_m is the measured thermal resistance for each experiment. (K/W)

q_{in} is the power supplied to the switch. (W)

ΔT is the differential temperature on opposing sides of switch. (K)

Three thermal resistance measurements are recorded at each distance setting with guard heater voltages of 10, 12 and 14 volts. The three measurements are averaged to

obtain a value for thermal resistance at each distance. Measurements are taken in 20µm increments up to 100 µm.

The parallel resistance accounting for heat losses from the test stand is calculated using a thermal circuit model, shown in Figure 3.1. The parallel resistance accounting for heat losses is denoted by R_p. The thermal resistance accounting for the conduction across the gas gap is denoted by R_c.

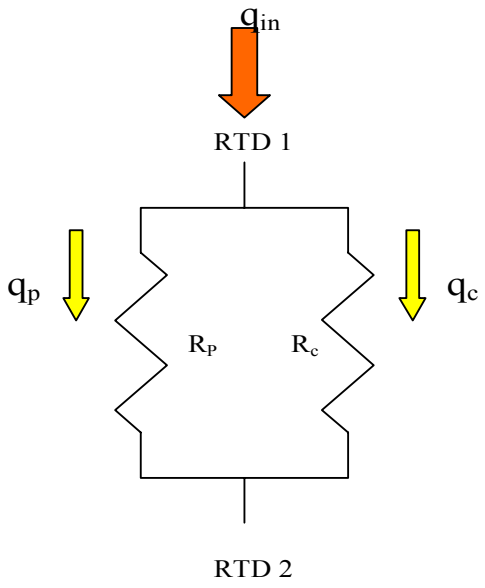

Figure 3.15: Thermal circuit model of parallel heat paths.

The total heat transfer for the circuit, denoted by q_{in}, is transferred through the parallel heat paths, q_p and q_c .

$$q_{in} = q_c + q_p \tag{3.5}$$

where: q_{in} is the total heat transferred across the gap.

q_c is the heat transferred by conduction across the gas gap.

q_p is the heat losses from the test stand or parallel heat path.

Since the heat transferred occurs over the same temperature difference, the equation can be written as:

$$\frac{\Delta T}{R_m} = \frac{\Delta T}{R_c} + \frac{\Delta T}{R_p} \tag{3.6}$$

Solving for R_p yields:

$$R_p = \frac{1}{\left(\frac{1}{R_m} - \frac{1}{R_c}\right)} \tag{3.7}$$

The parallel resistance is calculated using the averaged thermal resistance measurements at the each gap length. Graphs of the calibrations for the test stand with air and Xe atmospheres in the bell jar can be seen in Figures 3.16 and 3.17. The graphs show the measured thermal resistance of the gas layers versus gas layer thickness, L, in solid blue triangles. The thermal resistance across the gas layers predicted by equation 3.1 is shown with solid lines. The measured thermal resistance of the gas layer adjusted to account for the parallel heat loss is shown in open squares. The adjustment of the measured data is accomplished by fitting the measured data to the predicted thermal resistance. The fit is accomplished by searching for the parallel resistance that minimizes the sum of the squares of the residuals between the measured data and the predicted thermal resistance across the gas gap. The measured thermal resistances adjusted for the parallel heat loss is then the calibrated thermal resistance.

There is also an offset between the measured thermal resistance and the calculated thermal resistance. This offset can be seen at the initial measurement, taken at zero

distance, for each graph. The offset is a result of misalignment of experimental dies. Due to the scale of these distances minor misalignments create substantial changes in measured thermal resistance. The alignment affect is accounted for in the parallel resistance calculations by offsetting the measured values by the difference between the measured and calculated initial thermal resistance points.

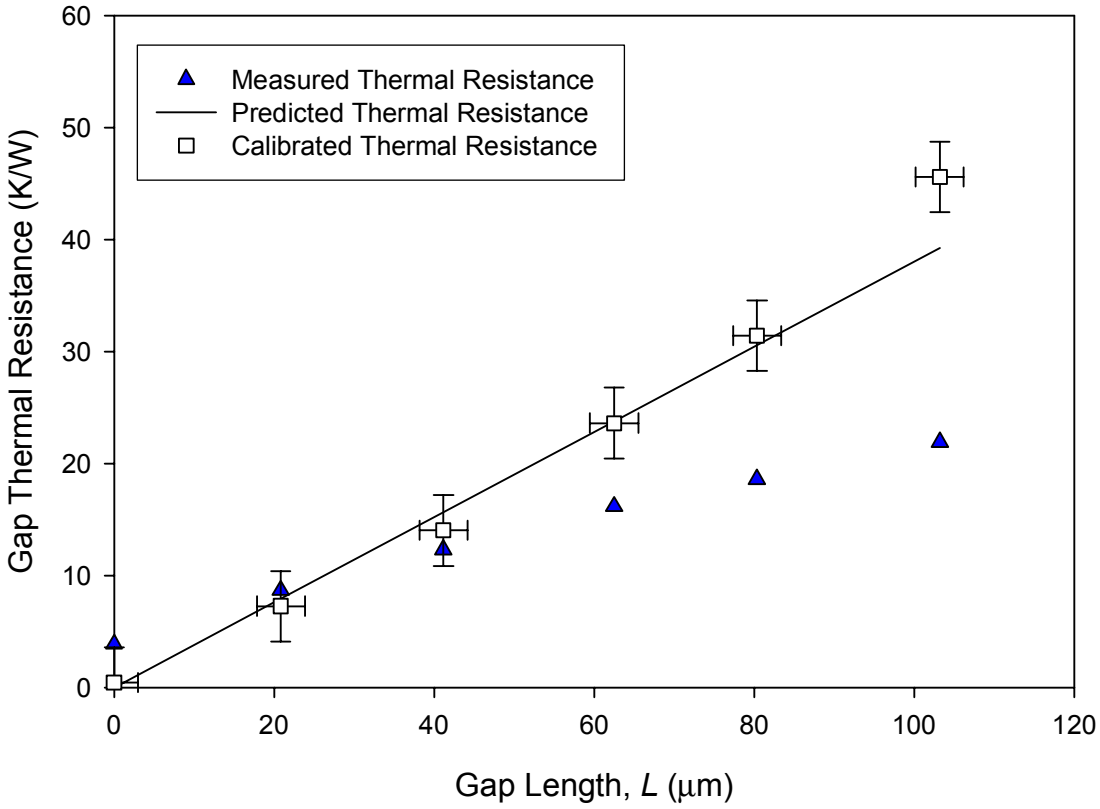

Figure 3.16: Test stand calibration for air.

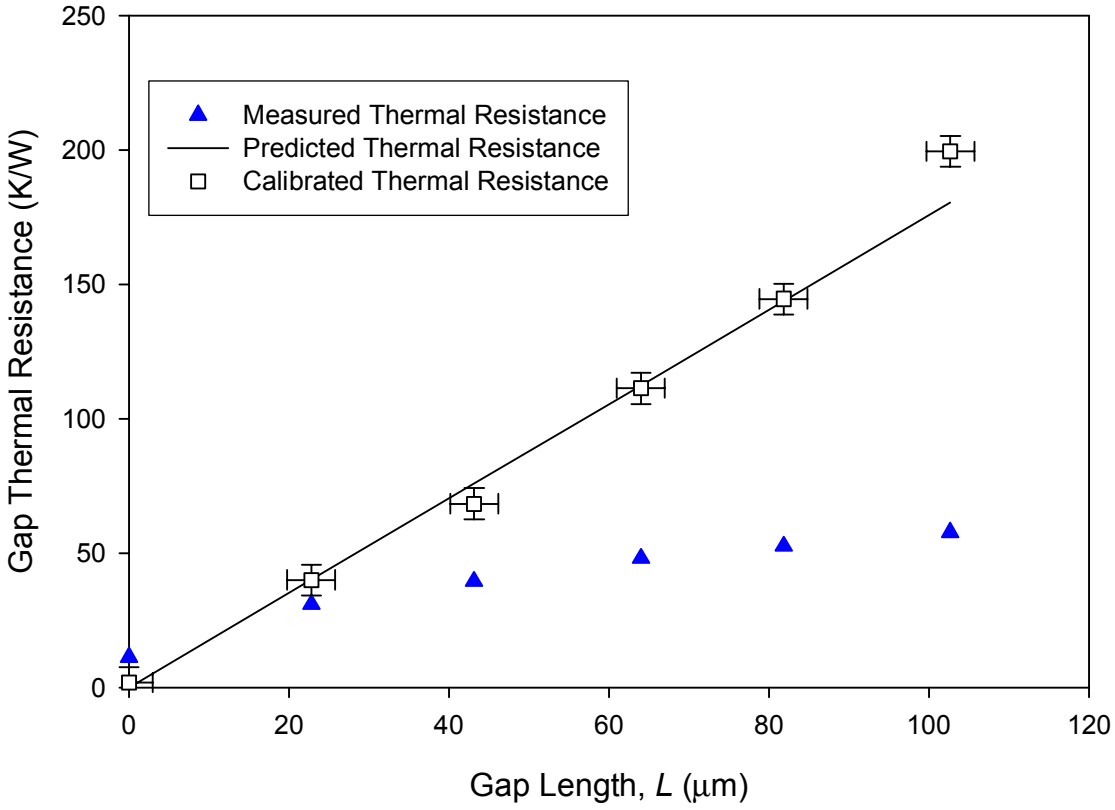

Figure 3.17: Test stand calibration for Xe.

The thermal resistance for low pressure (0.5 torr) air was calculated using an approximate method relating the heat transfer to the mean free path. This method is discussed in detail in Holman [34]. The result of the test stand calibration for the vacuum experimental condition is in Figure 3.18.

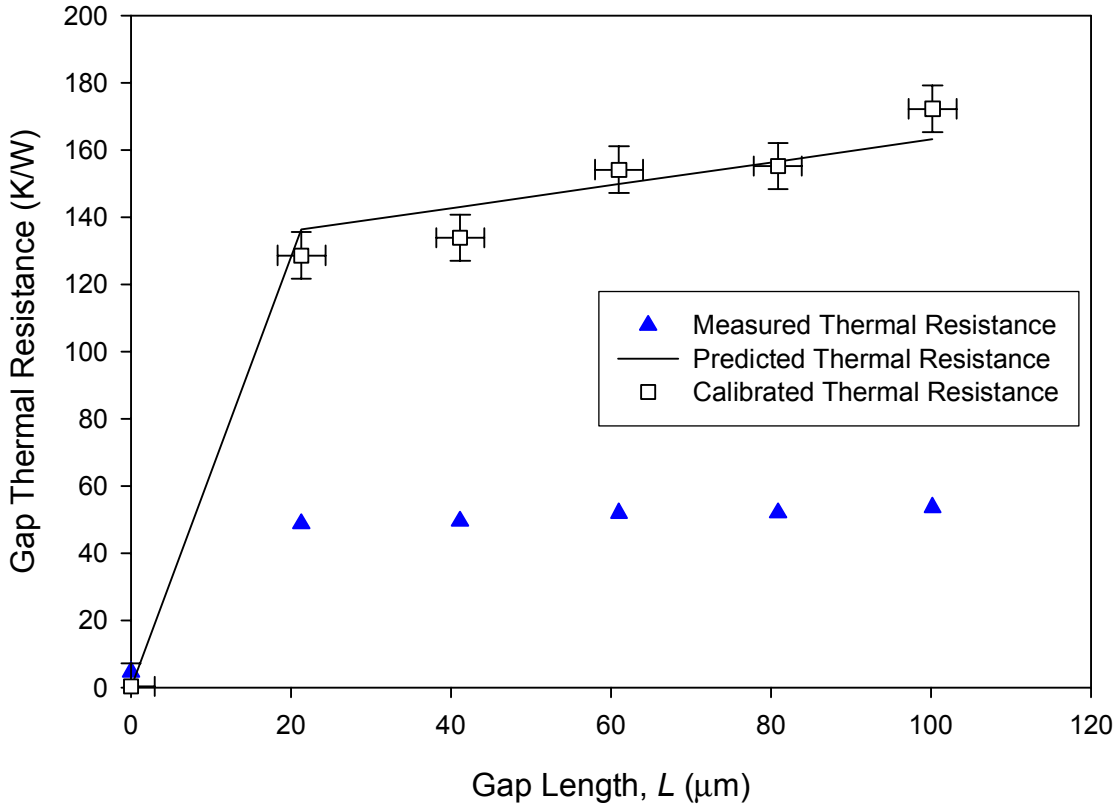

Figure 3.18: Test stand calibration for vacuum.

The test stand calibrations show that the measured thermal resistance can be fitted to the calculated thermal resistance through the addition of a parallel heat path. Generally the fitted data is within the error of uncertainty associated with the calculation of parallel resistance. At the largest gap distances the fitted data starts to deviate from the calculated values.

In each of the preceding calibrations, the measured data was adjusted to the predicted gas gap thermal resistance by fitting a parallel resistance, R_p. The values for the parallel resistance from these fits are summarized in Table 3.1. The variation in the parallel resistance is due to the various gas fills surrounding the test stand and their

relative ability to conduct heat. For example ambient air is a relatively good thermal conductor compared to air at 0.5 torr or xenon at ambient pressure resulting in a relatively low parallel resistance.

Experiment	Parallel Resistance (K/W)
Air (760 torr)	39.4
Xenon (760 torr)	82.0
Air(0.5 torr)	78.0

Table 3.1: Parallel resistance values for each fill gas.

3.3.2 Test Procedure

The experimental procedure to measure the thermal resistance across the mercury micro-droplet arrays is similar to the procedures describe above for the test stand calibration. A die with a mercury micro-droplet array is attached to the alignment die in place of the blank die. A load (~0.196 N) is applied and the RTD is zeroed out when the heat flux output is known to be zero. The guard heater is turned on to an initial setting of 10 V. The dies are separated a distance of approximately 100 μm. Each experiment starts with the largest gap length, which is then continuously decreased until the droplet array makes contact with the heater die. Gap length is decreased in increments of ~20 μm. Once contact is made the force applied to the micro-droplet array is continuously increased until the maximum load of ~100g is reached. Measurements are taken at 0, 10, 20, 30, 50 and 100 grams. The smaller increments of load are utilized at smaller applied loads in order to resolve changes in thermal resistance when the most variation occurs. Guard heater settings of 10, 12, and 14 V are used throughout the experiment.

For measurements made in xenon, care is taken to provide a pure xenon gas environment. Once the RTD has been zeroed, for the Xe experiment, the vacuum pump

is turned on. First, the tube to the tank of Xe is evacuated. Then the pressure in the bell jar is drawn to ~0.5 torr. At this point, the vacuum pump is turned off and the bell jar is isolated using a valve. Xenon is allowed to fill the bell jar. The vacuum gauges are watched to determine when the xenon pressure has reached ambient. A constant flow of xenon is applied throughout the experiment to pressurize the system slightly above atmospheric pressure, 760 torr. To achieve this pressure, a flow of 0.05 Lpm is maintained throughout the experiment.

For measurements made in low pressure air (0.5 torr) a slightly different procedure is followed. Once the RTD is zeroed out the vacuum pump is turned on. The first data point at ~100 μm is not taken until the vacuum reaches 0.5 torr. The vacuum pump runs throughout the entire experiment due to leaks in the vacuum system. The vacuum is checked prior to each measurement to ensure a constant pressure is maintained during the experiment.

3.4 UNCERTAINTY ANALYSIS

3.4.1 Temperature Difference

Temperature measurements are taken for RTD calibrations using a glass thermometer with a resolution of ±0.5º C. For a conservative estimate of uncertainty +/- 0.5º C will be used for calculations involving the ΔT measurement.

3.4.2 Thermal Power Measurement

The uncertainty in the q_{in} measurement is best described with

$$q_{in} = V_H \bullet \left(\frac{V_{10}}{R_{10}} \right) \tag{3.8}$$

where: q_{in} is the power dissipated in heater on the top die.

V_H is the voltage drop across the heater on the top die.

V_{10} is the voltage drop across the 10 Ω series resistor.

R_{10} is the resistance of the 10 Ω resistor in series.

$$U_{q_{in}} = \sqrt{\left(\left(\frac{\partial q_{in}}{\partial V_H} \bullet U_{V_H} \right)^2 + \left(\frac{\partial q_{in}}{\partial V_{10}} \bullet U_{V_{10}} \right)^2 + \left(\frac{\partial q_{in}}{\partial R_{10}} \bullet U_{R_{10}} \right)^2 \right)} \tag{3.9}$$

where: $U_{q_{in}}$ is the uncertainty of the power dissipated in heater on the top die.

U_{V_H} is the uncertainty in the voltage drop across input die heater.

$U_{V_{10}}$ is the uncertainty in voltage drop across 10 Ω series resistor.

$U_{R_{10}}$ is the uncertainty in 10 Ω resistor.

Taking the corresponding partial differential equations yields:

$$U_{q_{in}} = \sqrt{\left(\left(\frac{V_{10}}{R_{10}} \bullet U_{V_H} \right)^2 + \left(\frac{V_H}{R_{10}} \bullet U_{V_{10}} \right)^2 + \left(\frac{-V_H \bullet V_{10}}{R_{10}^{\,2}} \bullet U_{R_{10}} \right)^2 \right)} \tag{3.10}$$

The uncertainty of the voltage drop across the 10 Ω resistor and input heater is taken as ±0.0005 V. The uncertainty in the series resistor is ± 0.1 Ω. As an example if a voltage drop across the resistor of 1 V and a voltage drop across input heater of 10 V are assumed then the resulting uncertainty is:

$$U_{q_{in}} = \sqrt{\left(\left(\frac{1}{10} \bullet 0.0005 \right)^2 + \left(\frac{10}{10} \bullet 0.0005 \right)^2 + \left(\frac{-10 \bullet 1}{10^2} \bullet 0.1 \right)^2 \right)} \approx .010W \tag{3.11}$$

The heat input through the thermal switch has some uncertainty associated with the heat flux sensor. During experimentation points are taken when the heat flux sensor is zeroed which assumes that there is no heat loss from the back of the heater die. When the heat flux sensor reads ± 0.004mV it was assumed zeroed. With a sensor resolution of 20mV/(W/cm^2) an uncertainty of ± 0.2mW is estimated. For a conservative estimate of the uncertainty ± 0.4 mW will be used for calculations. The total uncertainty in the heat transfer through the device is the rms of the uncertainty in heat input and uncertainty in the heat flux sensor.

$$U_{q_t} = \sqrt{\left(U_{q_{in}}{}^2 + U_H{}^2\right)} \tag{3.12}$$

where: U_H is the uncertainty in the heat flux sensor.

U_{q_t} is the uncertainty in total heat transfer through switch.

As an example the rms of the heat input uncertainty from equation 3.11combined with the uncertainty of the heat flux sensor is:

$$U_{q_t} = \sqrt{\left(.01^2 + .004^2\right)} \approx 0.01077W \tag{3.13}$$

3.4.3 Thermal Resistance Measurement

The uncertainty associated with the measured thermal resistance is calculated by taking the partial derivatives of equation 3.4 which is

$$U_{R_m} = \sqrt{\left(\left(\frac{\partial R_m}{\partial \Delta T} \bullet U_{\Delta T}\right)^2 + \left(\frac{\partial R_m}{\partial q_{in}} \bullet U_{q_t}\right)^2\right)} \tag{3.14}$$

Taking the partial differential equations and substituting them into equation 3.14 yields the expression for corrected heat input as a function of the experimental parameters.

$$U_{R_m} = \sqrt{\left(\left(\frac{1}{q_{in}} \bullet U_{\Delta T}\right)^2 + \left(\frac{-\Delta T}{q_{in}^2} \bullet U_{q_t}\right)^2\right)} \tag{3.15}$$

For example assume the heat input, q_{in}, is 0.5 W and the ΔT is 5 K. The uncertainty for the ΔT measurement used for this example is 0.5 K. Applying these values to equation 3.15 gives the following uncertainty in the measured thermal resistance measurement.

$$U_{R_m} = \sqrt{\left(\left(\frac{1}{0.5} \bullet 0.5\right)^2 + \left(\frac{-5}{0.5^2} \bullet 0.0107\right)^2\right)} \approx 2.36 \, {}^{K}\!/_{W} \tag{3.16}$$

3.4.4 Parallel Thermal Resistance Measurement

Next the parallel resistance uncertainty is calculated. The measured thermal resistance, from test stand calibration, is fitted to the modeled resistance using the corresponding parallel resistance in Table 3.1. Residuals are calculated from the discrepancy between the measured thermal resistance and the fitted values. The student T distribution is used to calculate the 95% confidence interval for the test stand calibration.

For small sample sizes, n<30, the student T distribution must be used for uncertainty analysis [35,36]. The sample size for the test stand calibrations is six which corresponds to the six different gap lengths. The residuals of each data point were obtained using the fitted values for the measured thermal resistance. The standard

deviation of the residuals is then calculated. The 95% confidence interval is calculated using the following formula:

$$\mu = \bar{x} \pm t_{\alpha/2} \bullet \frac{S}{\sqrt{n}} \tag{3.17}$$

where: μ is the confidence interval.

$\bar{x}$ is the sample mean.

$t_{\alpha/2}$ is the student t value from the student t table.

S is the sample standard deviation.

n is the sample size.

The sample mean is zero for the residuals of the test stand calibration. The t value is obtained from a table where α =1-(confidence interval). For a 95% confidence interval and a sample size of 6, α = 0.05.

3.4.5 Corrected Thermal Resistance Measurements

The uncertainty for the corrected thermal resistance measurements is obtained using the following relationship.

$$R_c = \frac{1}{\frac{1}{R_m} - \frac{1}{R_p}} \tag{3.18}$$

where: R_c is the corrected thermal resistance measurement.

R_m is the measured thermal resistance.

R_p is the measured parallel resistance from test stand calibrations.

The corresponding equation for uncertainty follows.

$$U_{R_c} = \sqrt{\left(\left(\frac{\partial R_c}{\partial R_m} \bullet U_{R_m}\right)^2 + \left(\frac{\partial R_c}{\partial R_p} \bullet U_{R_p}\right)^2\right)} \tag{3.19}$$

Calculating the partial differential equation yields an equation of uncertainty in terms of experimental parameters.

$$U_{R_c} = \sqrt{\left(\left[\left(\frac{1}{R_m} - \frac{1}{R_p}\right)^{-2} \bullet \frac{1}{R_m^2} \bullet U_{R_m}\right]^2 + \left[-\left(\frac{1}{R_m} - \frac{1}{R_p}\right)^{-2} \bullet \frac{1}{R_p^2} \bullet U_{R_p}\right]^2\right)} \tag{3.20}$$

For the example calculation of uncertainty assume a parallel resistance of 70 K/W with an uncertainty of ±2.0 K/W. Using the corresponding values into equation 3.20 gives an estimate of uncertainty.

$$U_{R_c} = \sqrt{\left(\left[\left(\frac{1}{10} - \frac{1}{70}\right)^{-2} \bullet \frac{1}{10^2} \bullet 2.36\right]^2 + \left[-\left(\frac{1}{10} - \frac{1}{70}\right)^{-2} \bullet \frac{1}{70^2} \bullet 2.0\right]^2\right)} \approx 0.33 \, {}^{K}\!/_{W} \tag{3.21}$$

Chapter 4 RESULTS

4.1 Thermal Resistance in Air at Ambient Pressure

Thermal resistance measurements were made versus gap length for the thermal switch in the "off" position and versus applied force for the thermal switch in the "on" position. Thermal resistance results for the "off" switch are shown in Figure 4.1.

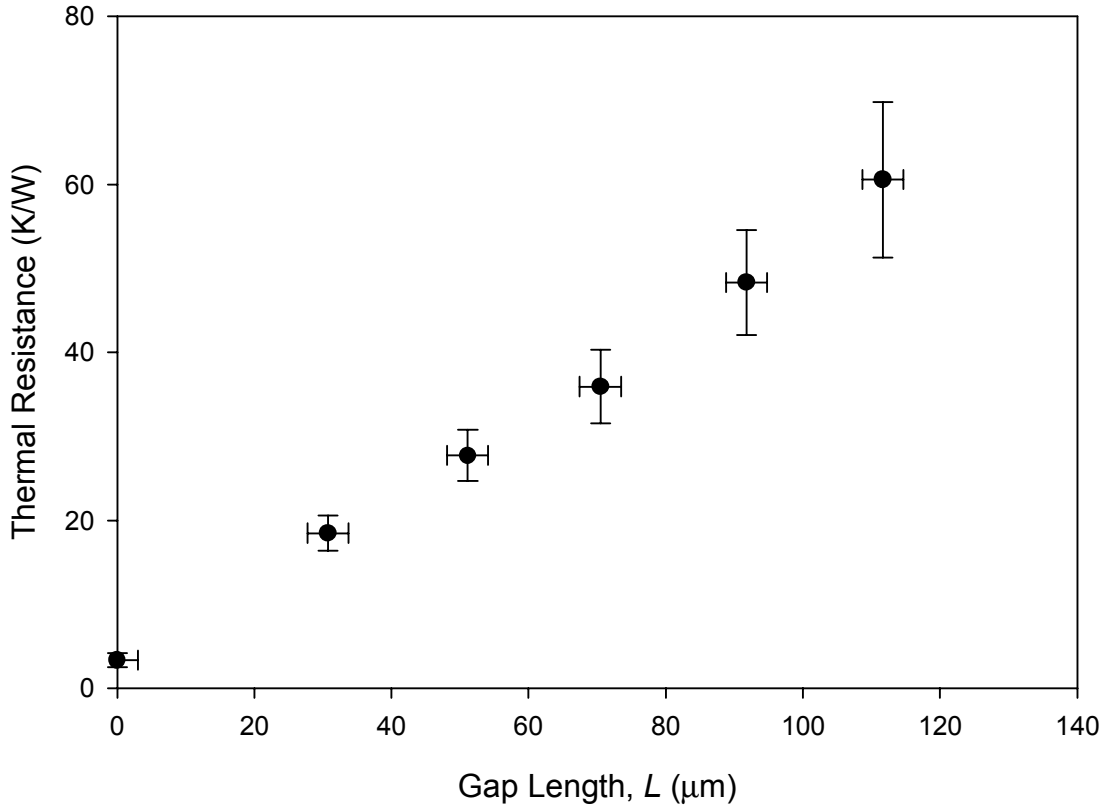

Figure 4.1: Thermal resistance vs. distance for 1600 droplet array in air.

When the thermal switch is in the "off" position, at 111μm, the switch thermal resistance is 60.5 K/W for heat transfer of ~0.2 W at a ΔT of 13K. The plot of resistance versus gap length is seen to be linear as expected for conduction heat transfer through air.

The "on" state of the thermal switch occurs when the mercury droplet array is in contact with the top die and a load is applied. Thermal resistance results for the "on" state are plotted versus applied load in Figure 4.2.

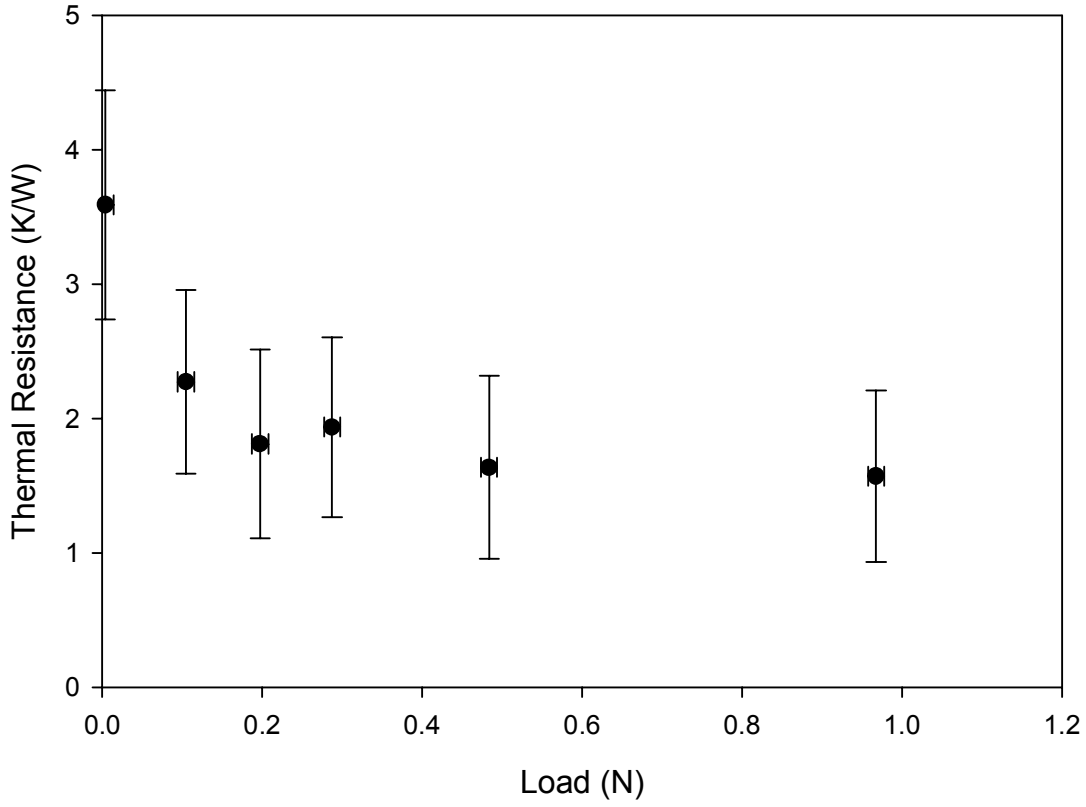

Figure 4.2: Thermal resistance vs. load for 1600 droplet array in air.

The largest applied load is approximately 1 N, at which load the micro-droplets deform the greatest amount. For this load of 0.968 N the thermal resistance of the switch is 1.57 K/W while transferring 1.03 W.

Once the mercury droplets come into contact with the top die there are two paths for conduction. One path is by conduction through the droplets. The other path is by conduction through the air.

4.2 Thermal Resistance in Xenon at Ambient Pressure

Thermal resistance measurements for a thermal switch filled with xenon at ambient pressure are shown in Figure 4.3. At the maximum gap length of 102μm the thermal resistance of the switch is 400 K/W while transferring 0.035 W across a ΔT of 14 K. This is the lowest amount of heat transfer for the three experiments.

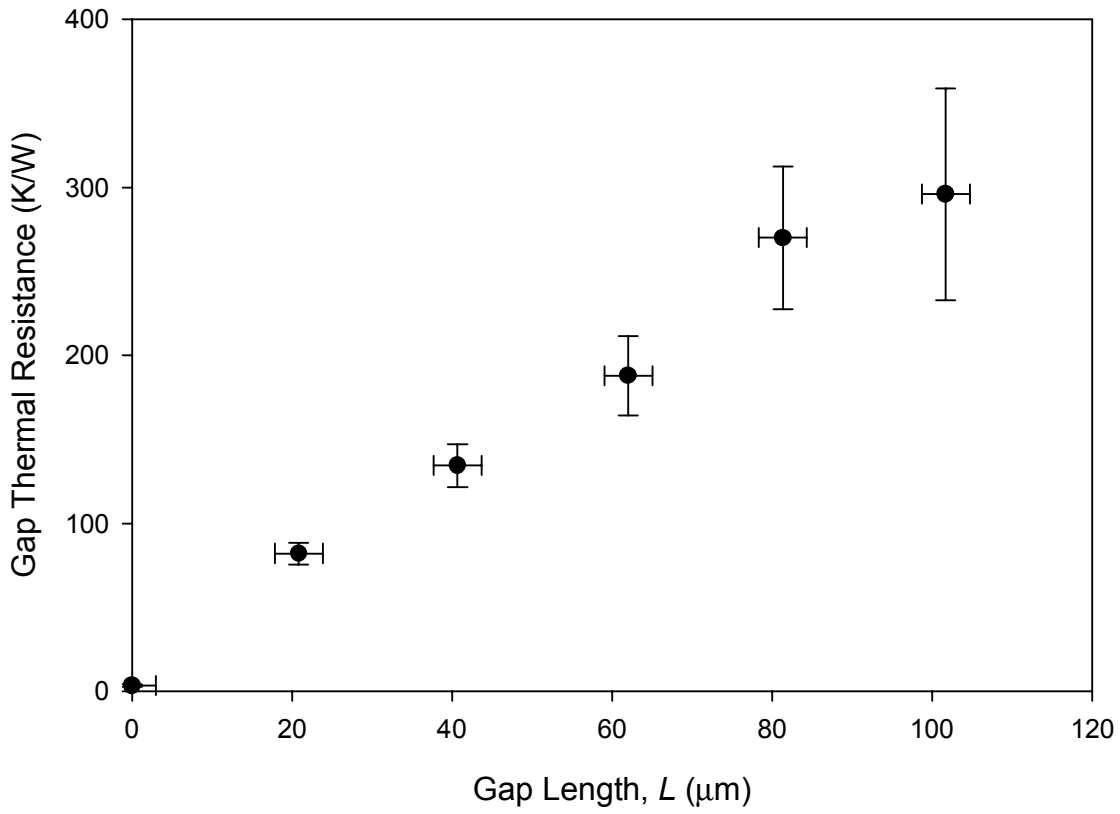

Figure 4.3: Thermal resistance vs. distance for 1600 droplet array in xenon.

The "on" state for the Xe experiment also shows higher thermal resistance than air at maximum load. Thermal resistance measurements for the "on" state of the thermal switch filled with xenon are shown in Figure 4.4. With an applied load of 1.02 N the thermal resistance of the switch is 1.95 K/W.

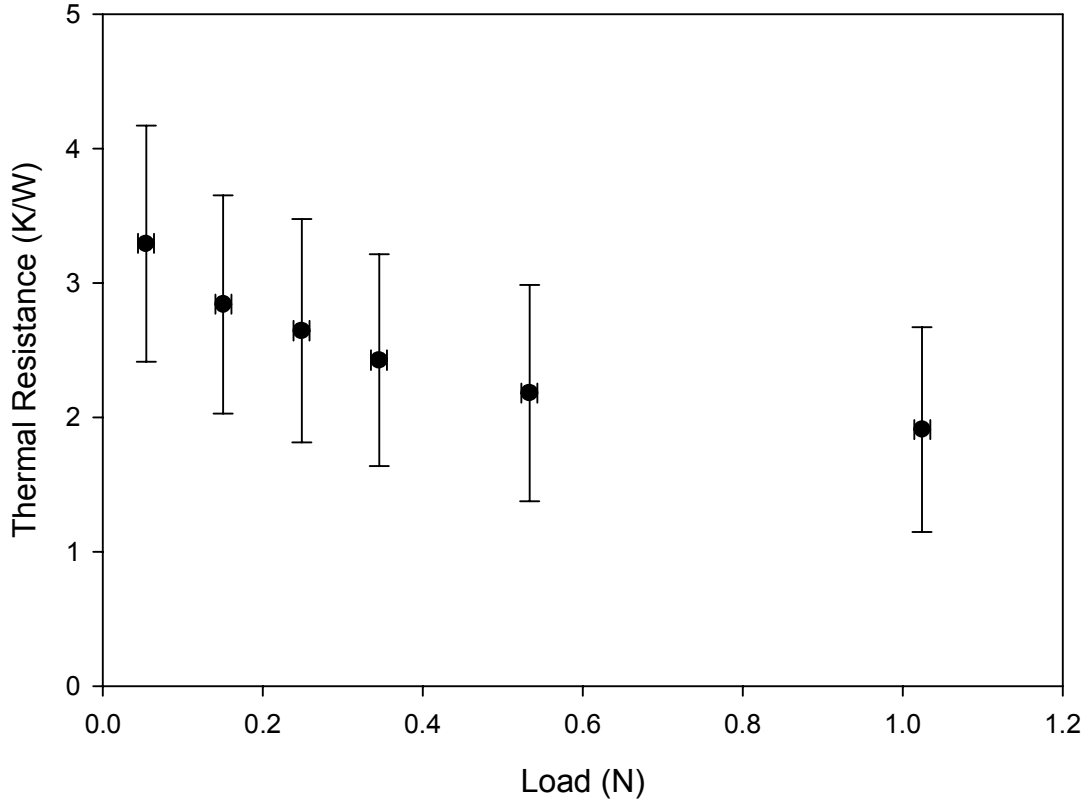

Figure 4.4: Thermal resistance vs. load for 1600 droplet array in xenon.

4.3 Thermal Resistance in Low Pressure Air

Thermal resistance measurements for a thermal switch filled with air at a pressure of 0.5 torr are shown in Figure 4.5. The measurements show a decrease of heat transfer in the "off" state compared to the air experiment. There is a substantial increase in

thermal resistance at smaller gap lengths.

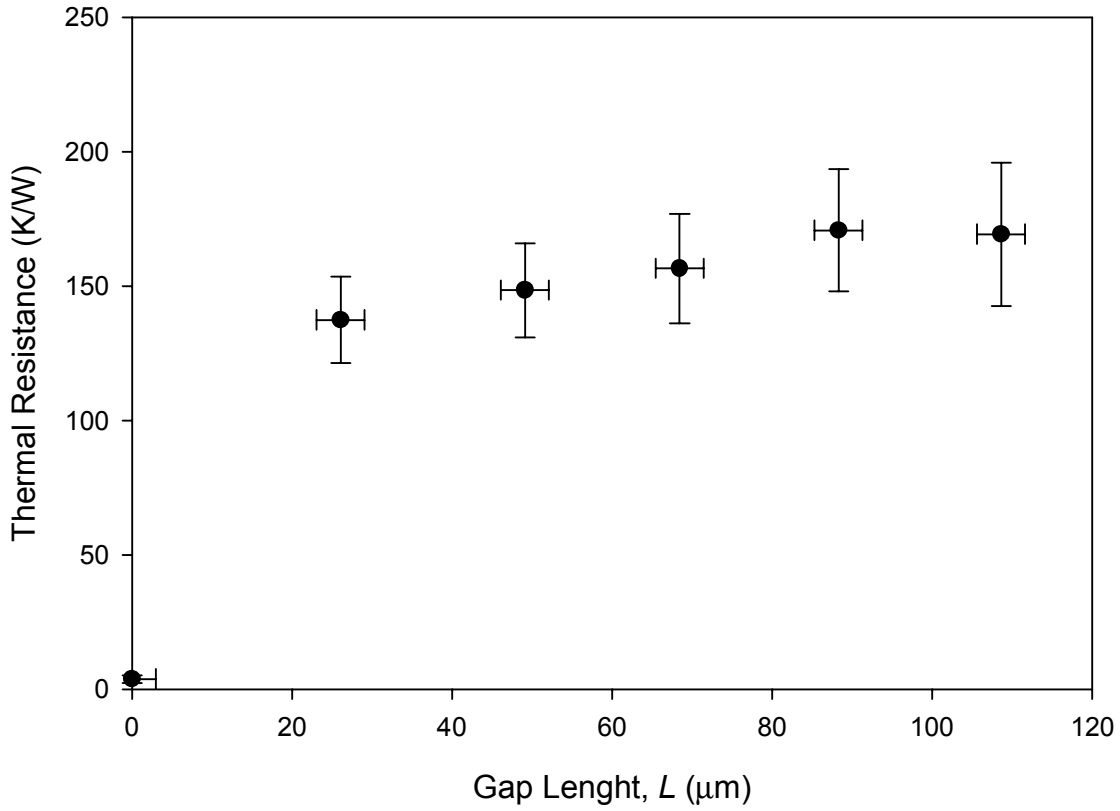

Figure 4.5: Thermal resistance vs. distance for 1600 droplet array in vacuum.

For a gap length of 108 μm the thermal resistance is seen to be 169 K/W while the switch transfers 0.07 W over a ΔT of 12 K. This thermal resistance is 3 times less than for air at a comparable distance of 111μm. The plot shows a large change in thermal resistance as the mercury droplet die moves from contact with the top die to a gap length of ~20 μm. This large change in thermal resistance happens over a very short distance compared to the air experiment.

Thermal resistance measurements for the "on" position, when the thermal switch is filled with low pressure air, is shown in Figure 4.6.

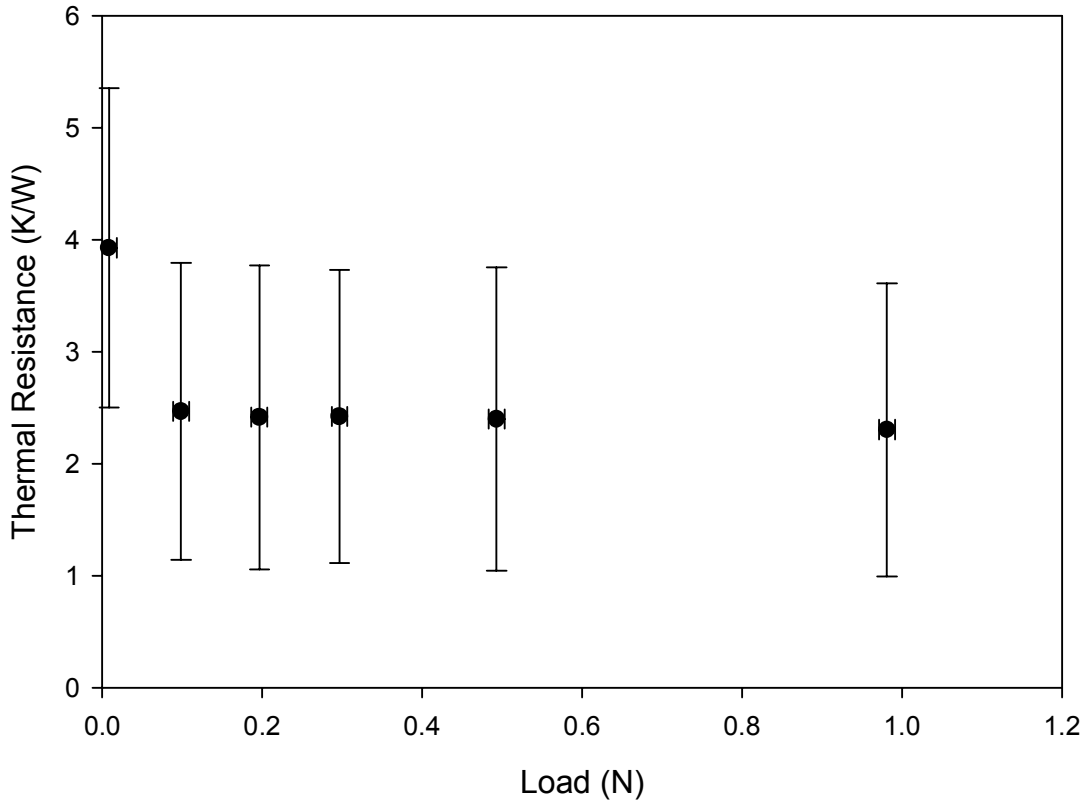

Figure 4.6: Thermal resistance vs. load for 1600 droplet array in vacuum.

Less heat is transferred for comparable conditions in low pressure air than ambient air. For a load of 0.98 N the thermal resistance is 2.3 K/W while the switch transfers 0.31W over a ΔT of 0.7 K. This increase in thermal resistance is the result of the parallel heat path through the air being diminished by the reduction in air pressure.

The kinetic theory of gases is used to explain the conductivity of gases [33]. The thermal conductivity is directly proportional to the number of particles per unit volume *n,* the mean molecular speed $\dot{c}$, and the mean free path λ. The mean free path is the average distance molecules travel between collisions. The thermal conductivity is described with

$$k \propto n\dot{c}\lambda \tag{4.1}$$

The mean molecular speed increases with temperature and decreases with molecular weight. Therefore the thermal conductivity increases with decreasing molecular weight. This is why higher thermal resistance measurements are obtained for the experiment with xenon at 760 torr than air at 760 torr.

The thermal resistance measurements from the experiment in air at 0.5 torr shows a sharp increase in thermal resistance due to the decrease in the mean free path distance up to 25 μm. The change in thermal resistance becomes smaller over comparable gap length changes after this distance. For gap lengths larger than the mean free path distance only a small amount of increase in the thermal resistance for increasing gap length is measured.

Chapter 5 CONCLUSIONS

5.1 Heat Transfer

The ability to control heat transfer in MEMS is important for many applications. This ability to control heat transfer rates using a thermal switch has been shown in the present set of experiments.

When the switch is "off" with gap lengths of ~100 μm the thermal resistance of the switch is 296 K/W for the switch in xenon at ambient pressure, followed by a thermal resistance of 169 K/W for the thermal switch with 0.5 torr air and then the switch in ambient air at 60.5 K/W.

The most heat is transferred when the mercury micro-droplet arrays are pressed against the top die. At the maximum load of ~1 N the switch is "on" and the lowest thermal resistance is for air at ambient pressure, 1.57 K/W, followed by xenon at ambient pressure, 1.90 K/W, an air at 0.5 torr, 2.3 K/W. An ideal switch would transfer the least amount of heat in the "off" position and the most amount of heat in the "on" position.

The highest rate of heat transfer for the "on" position is for a switch filled with air at ambient pressure. This high heat transfer rate is due to the parallel heat paths through the mercury droplet array and air. The conductivity of air is larger than that of Xe. One way to decrease this thermal resistance would be to increase the number of droplets to enlarge the contact area for the droplets when the switch is in the "on" position.

The gap length required to shut the switch off is an important parameter. Displacing a thermal switch 100 μm in a micro-scale device is difficult. A deflection between 20 to 30 μm would be much easier to realize in a practical device. One effective

way to compare the switching ability of a thermal switch is through the non-dimensional "off" to "on" thermal resistance ratio. The thermal resistance ratios are presented in Table 5.1. For comparison, gap lengths of 26 and 88 μm were chosen. Thermal resistance measurements were taken at these distances for the vacuum experiment. The ratios for air and xenon were approximated by interpolating the data to obtain values of thermal resistance at 26 and 88 μm. At an 88 μm gap distance the highest ratio is seen for the thermal switch filled with xenon. For the shorter gap distance of 26 μm the best ratio or R_{off}/R_{on} is for the thermal switch filled with 0.5 torr air.

Medium	"off" Distance of 26 μm	"off" Distance of 88 μm
Air (760 torr)	10	30
Xenon(760 torr)	50	143
Air (0.5 torr)	60	74

Table 5.1: Comparison of "off" to "on" thermal resistance ratios.

5.2 Recommendations

Three aspects of the test stand apparatus could be improved upon to increase the repeatability and accuracy of the thermal resistance measurements. Alignment of the dies is a critical parameter for accurate thermal resistance measurements at small gap distances. The gap distance measurements could be improved upon to decrease the uncertainty in the measurements as well. Finally the vacuum system has a small leak, that, if fixed would prevent unnecessary waste.

Alignment of the silicon dies is accomplished with a two part epoxy and the application of pressure until the dies come into complete contact. Aligning the dies with a mechanical device which could compensate for misalignment would be very beneficial. There is a need for something that is more reproducible, which would enhance the accuracy of the test stand.

The current setup uses a stepper motor and controller to obtain measurements of displacement. These measurements are affected by the stabilizing apparatus on the test stand. When the direction of displacement is switched the readout can be off as much as 50 μm. If the direction is reversed again you are able to return to the initial point with an accuracy or ± 0.5 μm. Clearly there is binding due to the stabilizer plate. The stabilizer plate is necessary for the current setup to prevent the heat sink from moving laterally. The linear stages decreased stability is due to the mechanical amplification of the adapter plate, load cell and heat sink. Rearranging these pieces so they are not attached to the linear stage would decrease the moment arm thus increasing the stability

Currently the vacuum system requires the pump running throughout the full experiment when experimenting in a vacuum environment. This is due to leaks in the vacuum system. One possible source of leaking is the multiple connections in the manifold that are unnecessary. Minimizing the number of fittings in the system should decrease the amount of leaks.

Overall the experimental setup works adequately. The uncertainty in the measurement is quantifiable however improvements could be made. The suggested improvements would make the apparatus user friendly and more repeatable.

REFERENCES

[1]S. Whalen, M. Thompson, D.F. Bahr, C.D. Richards, R.F. Richards, "Design, Fabrication, and Testing of the P^3 Micro Heat Engine", *Sensors and Actuators A:Physical,* v. 104, n 3, pp.290-298

[2]Whalen, S.A., Thompson, M.R., Richards, C.D., Bahr, D.F., Richards, R.F., 2002, "Low Frequency Operation of The P3 Micro Heat Engine," in ASME International Mechanical Engineering Congress and Exposition, ASME, pp. 469-475.

[3]Christensen, A.O., 2003, "Fabrication and Characterization of Liquid-metal Micro-droplet Thermal Switch," Masters of Science in Mechanical Engineering, Washington State University, U.S.A.

[4] Bolz, R.E., Tuve, G.L., 200, *CRC Handbook of Tables for Applied Engineering Science,* Second, CRC Press Inc., Boca Raton Florida.

[5]Ruf,T., Henn, R.W., Asen-Palmer, M., Gmelin,E., Cardona, M., Pohl, H.-J., Devyatych, G.G., Sennikov, P.G., 2000," Thermal Conductivity of Isotopically Enriched Silicon," *Solid State Communications*, **115,** pgs. 243-247.

[6]Attaf, N., Aida, M.S., Hadjeris, L., 2001, "Thermal Conductivity of Hydrogenated Amorphous Silicon," *Solid State Communications,* **120**, pgs. 525-530.

[7] Volz, S., Lysenko, V., 2000, " Porous Silicon Thermal Conductivity by Scanning Probe Micrsocopy," *Phys. Stat. Sol.,* **182,** pgs. R6-R7.

[8]Amata, G., Angelucci, R., Benedetto, G., Boarino, L., Dori, L., Maccagnani, P., Rossi, A.M., Spagnolo, R., 2000, " Thermal Characterization of Porous Silicon Membranes," *Journal of Porous Materials,***7,** pgs. 183-186.

[9]Benedetto, G., Boarino, L., Spagnolo, R., 1997, " Evaluation of Thermal Conductivity of Porous Silicon Layers by a Photoacoustic Method," *Applied Physics A,* **64,** pgs. 155-159.

[10]Burzo, M.G., Komarov, P.L., Raad, P.E., 2002, " Thermal Transport Properties Of Gold-Covered Thin-Film Silicon Dioxide," *Inter. Society Conference on Thermal Phenomena*, IEEE, pgs. 142-149.

[11]Launay, S., Sartre, V., Lallemand, 2004, " Experimental Study on Silicon Micro-Heat Pipe Arrays," *Applied Thermal Engineering,* **24,** pgs. 233-234.

[12]Xu, J., Fisher, T.S., 2004, "Enhanced Thermal Contact Conductance Using Carbon Nanotube Arrays," *International Society Conference on Thermal Phenomena,* IEEE, pgs. 549-555.

[13]Ang, C.S., Tan, H.S., Chan, S.L., 1973, "Three-Layer Thermal-Diffusivity Problem Applied to Measurements on Mercury," *Journal of Applied Physics,* **44,** No. 2, pgs. 687-691.

[14]Nagai, H., Rossignol, F., Nakata, Y., Tsurue, T., Suzuki, M., Okutani, T., 2000, " Thermal Conductivity Measurment of Liquid Materials by a Hot-Disk Method in Short-Duration Microgravity Environments," *Material Science and Engineering,* **A276,** pgs. 117-123.

[15]Ould-Lahoucine, C., Sakashita, H., Kumada, T., 2003, " A Method For Measureing Thermal Conductivity of Liquids and Powders With a Thermistor Probe," *Int. Comm. Heat Mass Transfer,***30,** No.4, pgs 445-454.

[16]Fletcher, L.S., 1988, "Recent Developments in Contact Conductance Heat Transfer", *Journal of Heat Transfer*, **Vol. 110,** pgs. 1059-1070.

[17]Li, Y.Z., Madhusudana, C.V., Leonardi, E., 2000, " On the Enhancementof the Thermal Contact Conductance: Effect of Loading History," *Journal of Heat Transfer*, **122**, February, pgs. 46-49.

[18]McWaid, T., Marschall, E., 1992, "Thermal Contact Resistance Across Pressed Metal Contacts in a Vacuum Environment", *International Journal Heat and Mass Transfer*, **Vol. 35 No. 11**, pgs. 2911-2920.

[19]Wahid, S., Madhusudana, C.V., 2000, "Gap Conductance in Contact Heat Transfer", *International Journal of Heat and Mass Transfer,* **Vol. 43,** pgs. 4483-4487.

[20]Peterson, G.P., Fletcher, L.S., 1988, "Thermal Contact Conductance of Packed Beds in Contact With a Flat Surface", *ASME*, **Vol. 110**, February, pgs. 38-41.

[21]Y. Liu, X. Li, T. Abe, Y. Haga, M. Esashi, 2001, "A Thermomechanical Relay with Microspring Contact Array", Proceedings of the 14th IEEE International Conference on Micro Electro Mechanical Systems, pgs. 220-223.

[22]Be'er, A., Lereah, Y., Frydman, A., Taitelbaum, H., 2002, " Spreading of a Mercury Droplet on Thin Gold Films," *Physica A,* **314,** pgs. 325-330.

[23]Smith, E.N., Parpia, J.M., Beamish, J.R., 2000," A ^{3}He Gas Switch for the 0.5-2K Temperature Range," *Physica B 284-288,* pp. 2026-2027

[24]Prina, M., Kulleck, J.G., Bowman Jr., R.C., 2002, " Assessment of Zr-V-Fe getter alloy for gas-gap heat switches", *Journal of Alloys and Compounds*, pp. 886-891.

[25]Glaister, D.S., Curran, D.G.T., Mahajan, V.N., 1996, " Application of Cryogenic Thermal Switch Technology to Dual Focal Plane Concept for Brilliant Eyes Sensor Payload", IEEE, **v.2,** pages 115-127.

[26]Milanez, F.H., Mantelli, M.B.H., 2003, " Theoretical and experimental studies of a bi-metallic heat switch for space applications," *International Journal of Heat and Mass Transfer,* **v.46**, pages 4573-4586.

[27]Beasley, M.A., Firebaugh, S. L., 2004,"Design and Packaging for a Microelectromechanical Thermal Switch Radiator," *Inter Society Conference on Thermal Phenomenon*,

[28]Slater, T., Van Gerwen, P., Masure, E., Preud'homme, F., Baert, K., 1995, " Thermo-Mechanical Characteristics of a Thermal Switch," *8th International Conference on Solid-State Sensors and Actuators*, Stockholm Sweden, pgs. 341-344

[29] L. Latorre, J. Kim, P. Nouet, 2000, "CJ" Kim, "Electrostatic Actuation of Microscale Liquid Metal Droplets: Analysis, Experiment, and FEM Simulation", *MEMS* **2**, 105-110

[30] Crain, K.R., 2005," Mechanical Characterization and Thermal Modeling of a MEMS Thermal Switch",M.S., Washington State University, U.S.A.

[31]Occupational Safety and Health Administration: "Table Z1 – Limits for Air Contaminants – 1910.1000", http://www.osha.gov/pls/oshaweb

[32] Cho, J.H.., 2004,"Electro-Mechanical Characterization of Piezoelectric MEMS Power", M.S., Washington State University, U.S.A.

[33]Incropera, F.P., DeWitt, D.P., 2002, *Introduction to Heat Transfer*, Fourth, John Wiley & Sons, New York.

[34]Holman, J.P.,1997, *Heat Transfer,* Eighth, McGraw-Hill, pg. 368.

[35]Wheeler, A.J., Ganji, A.R.,1996, *Introduction to Engineering Experimentation*, Prentice Hall, New Jersey.

[36]Devore, J.L., 2004, *Probability and Statistics for Engieering and the Sciences*, Sixth, Thomson Brooks/Cole, California.

APPENDIX

Test Stand Calibration, Ambient Pressure Air		
Distance	Delta T	Uncorrected Power
(μm)	(K)	(W)
0.00	0.00	0.00
0.00	1.35	0.35
0.00	2.11	0.54
0.00	2.99	0.75
20.84	0.00	0.00
20.84	6.14	0.70
20.84	5.03	0.57
20.84	3.70	0.44
41.18	0.00	0.00
41.18	4.66	0.39
41.18	6.20	0.50
41.18	8.21	0.65
62.50	0.00	0.00
62.50	9.97	0.62
62.50	8.15	0.50
62.50	6.19	0.38
80.37	0.00	0.00
80.37	6.49	0.35
80.37	8.29	0.45
80.37	10.84	0.58
103.19	0.00	0.00
103.19	12.10	0.56
103.19	9.94	0.45
103.19	7.70	0.35

Temperature Differential vs. Power Input for Test Stand Calibration in Ambient Pressure Air

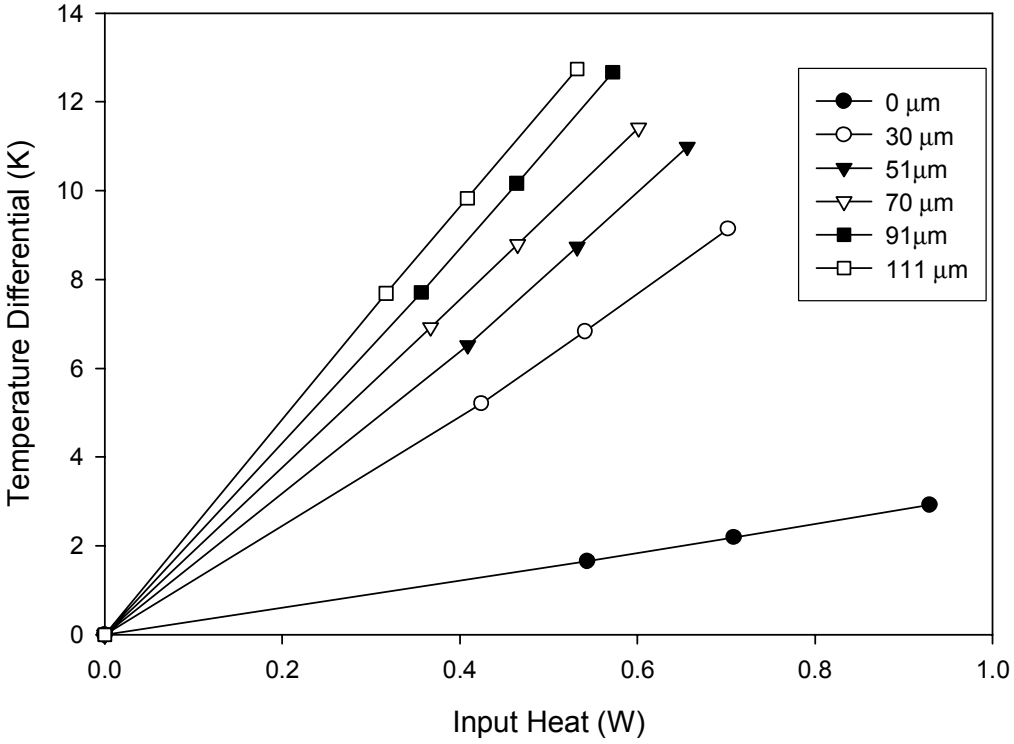

Test Stand Calibration, Ambient Pressure Xenon

Load	Delta T	Uncorrected Power
(N)	(K)	(W)
1.01	0.00	0.00
1.01	1.94	0.25
1.01	3.30	0.40
1.00	4.73	0.55
0.50	0.00	0.00
0.50	4.30	0.52
0.50	3.74	0.44
0.51	3.03	0.35
0.02	0.00	0.00
0.02	3.14	0.30
0.02	4.48	0.38
0.02	6.09	0.49
Distance	Delta T	Uncorrected Power
(μm)	(K)	(W)
22.82	0.00	0.00
22.82	12.09	0.39
22.82	10.53	0.34
22.82	8.20	0.27
43.16	0.00	0.00
43.16	9.23	0.24
43.16	11.37	0.29
43.16	14.42	0.36
64.00	0.00	0.00
64.00	16.40	0.35
64.00	14.08	0.29
64.00	11.15	0.23
81.86	0.00	0.00
81.86	11.50	0.21
81.86	13.73	0.26
81.86	16.86	0.32
102.69	0.00	0.00
102.69	18.08	0.32
102.69	15.68	0.27
102.69	12.47	0.21

Temperature Differential vs Input Power for Test Stand Calibration in Ambient Pressure Xenon

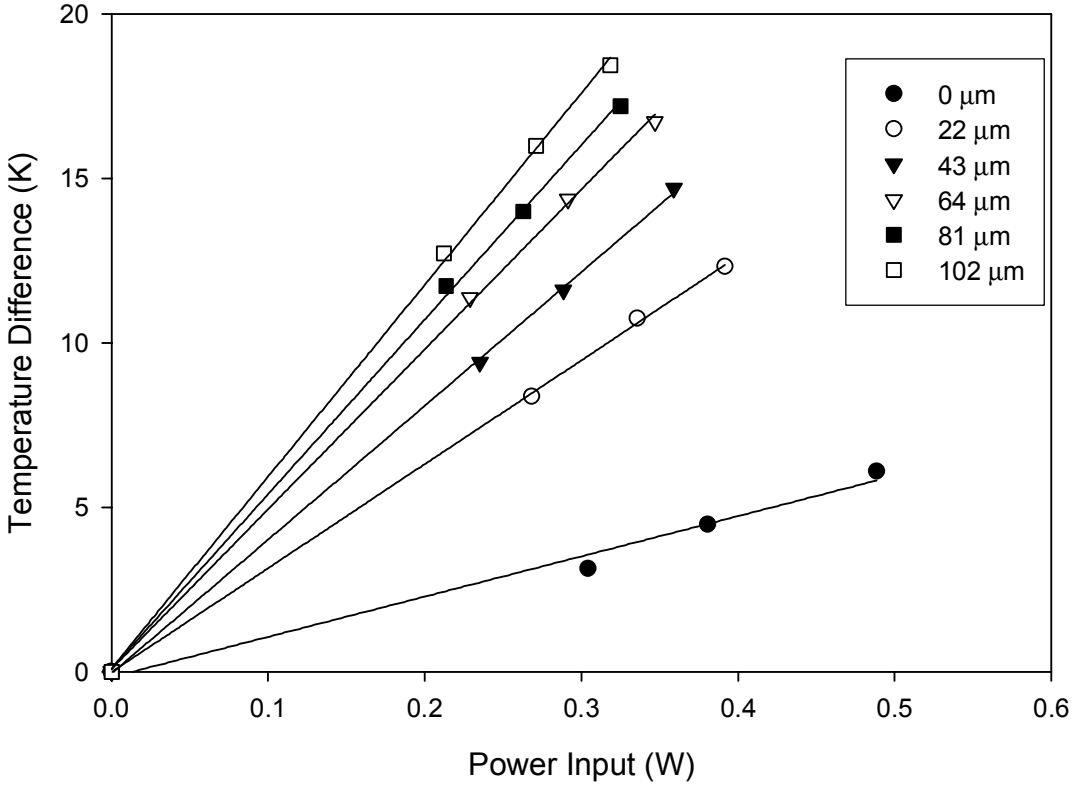

Test Stand Calibration, 0.5 torr Air		
Load	Delta T	Uncorrected Power
(N)	(W)	(K)
1.00	0.00	0.00
1.00	0.66	0.21
1.00	0.89	0.29
1.00	1.18	0.38
0.52	0.00	0.00
0.52	1.34	0.39
0.52	1.11	0.32
0.53	0.88	0.25
0.00	0.00	0.00
0.00	1.04	0.22
0.00	1.30	0.27
0.00	1.69	0.36
Distance	Delta T	Uncorrected Power
(μm)	(K)	(W)
21.33	0.00	0.00
21.33	17.46	0.36
21.33	14.47	0.30
21.33	11.28	0.23
41.18	0.00	0.00
41.18	11.01	0.22
41.18	13.64	0.28
41.18	17.32	0.35
61.02	0.00	0.00
61.02	18.67	0.36
61.02	15.33	0.29
61.02	11.76	0.22
80.86	0.00	0.00
80.86	11.53	0.22
80.86	14.19	0.28
80.86	17.83	0.35
100.21	0.00	0.00
100.21	18.62	0.35
100.21	15.44	0.29
100.21	12.23	0.23

Temperature Differential vs. Power Input for Test Stand Calibration in 0.5 torr Air.

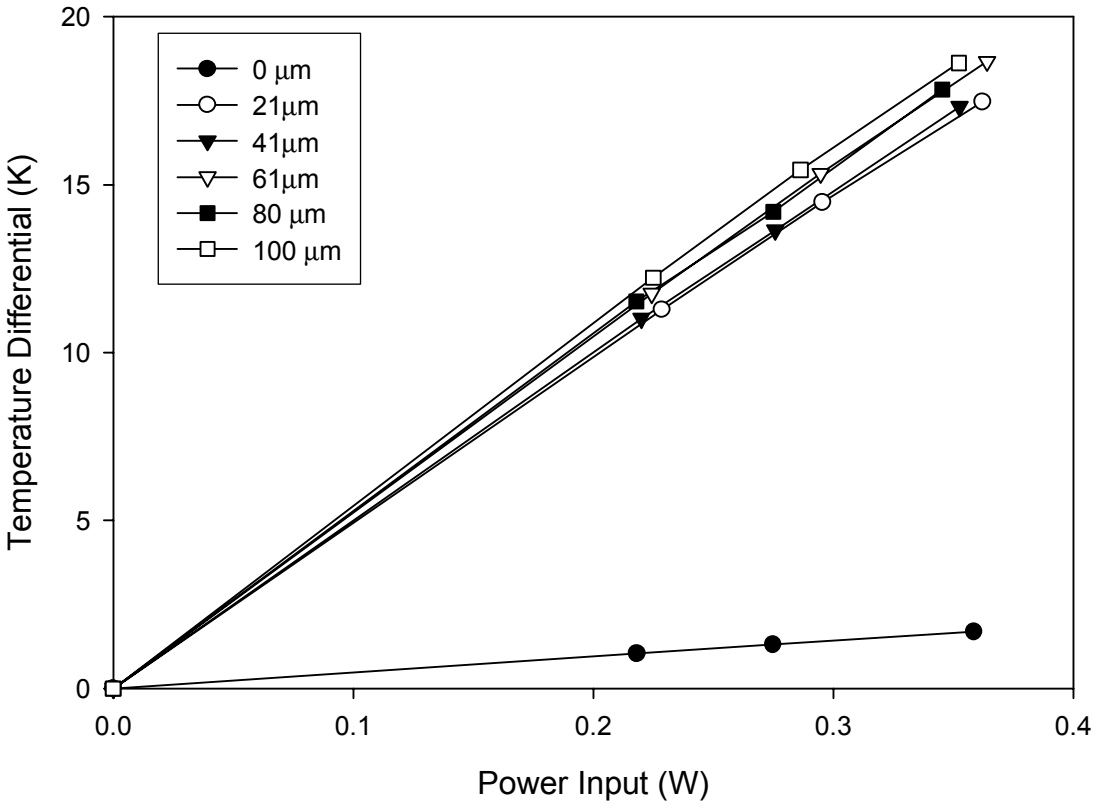

1600 Droplet Experiment in Ambient Pressure Air

Distance	Delta T	Uncorrected Power	Load	Delta T	Uncorrected Power
(μm)	(K)	(W)	(N)	(K)	(W)
30.76	0.00	0.00	0.00	0.00	0.00
30.76	5.20	0.42	0.00	1.65	0.54
30.76	6.83	0.54	0.00	2.19	0.71
30.76	9.14	0.70	0.00	2.92	0.93
51.10	0.00	0.00	0.10	0.00	0.00
51.10	10.99	0.66	0.10	1.20	1.01
51.10	8.73	0.53	0.10	0.68	0.79
51.10	6.52	0.41	0.10	0.32	0.60
70.45	0.00	0.00	0.20	0.00	0.00
70.45	6.92	0.37	0.20	0.28	0.59
70.45	8.80	0.47	0.20	0.59	0.75
70.45	11.42	0.60	0.20	0.96	0.98
91.78	0.00	0.00	0.29	0.00	0.00
91.78	12.67	0.57	0.29	0.93	1.01
91.78	10.16	0.46	0.29	0.55	0.80
91.78	7.71	0.36	0.29	0.17	0.60
111.62	0.00	0.00	0.49	0.00	0.00
111.62	7.69	0.32	0.49	0.14	0.60
111.62	9.83	0.41	0.48	0.43	0.76
111.62	12.74	0.53	0.48	0.78	1.00
			0.97	0.00	0.00
			0.97	0.68	1.04
			0.97	0.33	0.83
			0.97	0.05	0.63

Temperature Differential vs Input Power for Mercury Droplet array, in ambient Air, for Gap

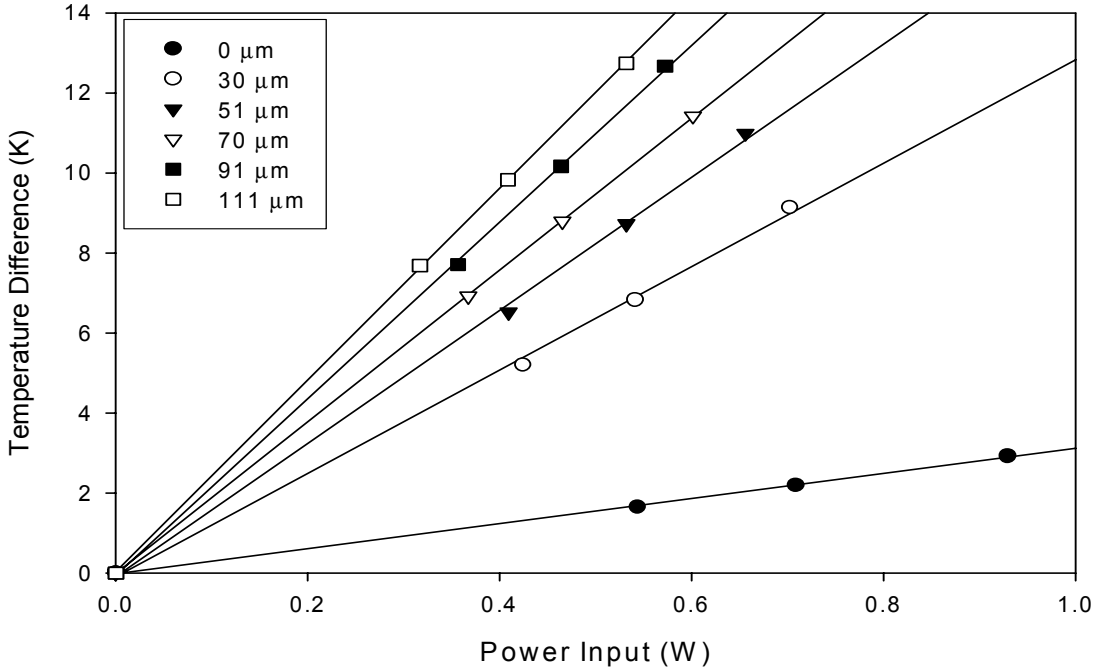

Temperature Differential vs. Power Input for Mercury Droplet Array, in Ambient Air, with Applied Load

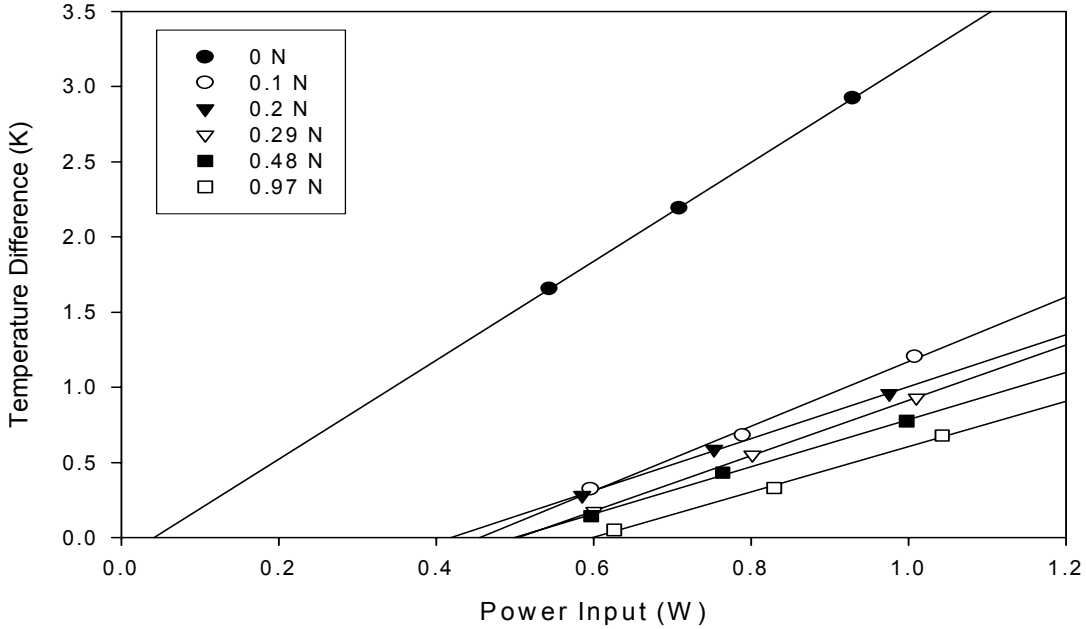

1600 Droplet Experiment in Ambient Pressure Xenon

Distance	Delta T	Uncorrected Power	Load	Delta T	Uncorrected Power
(μm)	(K)	(W)	(N)	(K)	(W)
20.84	0.00	0.00	0.05	0.00	0.00
20.84	11.56	0.28	0.05	1.54	0.51
20.84	14.11	0.34	0.05	2.01	0.65
20.84	18.02	0.43	0.06	2.62	0.74
40.68	0.00	0.00	0.15	0.00	0.00
40.68	20.37	0.39	0.15	2.51	0.85
40.68	17.09	0.33	0.15	1.90	0.68
40.68	13.31	0.26	0.15	1.40	0.52
62.02	0.00	0.00	0.25	0.00	0.00
62.02	13.03	0.22	0.25	1.31	0.51
62.02	15.97	0.28	0.25	1.72	0.65
62.02	20.24	0.35	0.25	2.23	0.84
81.36	0.00	0.00	0.34	0.00	0.00
81.36	20.34	0.32	0.34	2.17	0.86
81.36	17.55	0.27	0.35	1.66	0.69
81.36	13.96	0.22	0.35	1.22	0.54
101.70	0.00	0.00	0.53	0.00	0.00
101.70	9.42	0.14	0.53	1.12	0.52
101.70	13.79	0.21	0.53	1.45	0.67
101.70	19.46	0.30	0.53	1.86	0.84
			1.03	0.00	0.00
			1.03	1.76	0.88
			1.03	1.34	0.71
			1.02	0.99	0.55

Temperature Differential vs Power Input for Mercury Droplet Array, Xenon at Ambient Pressure, for Gap

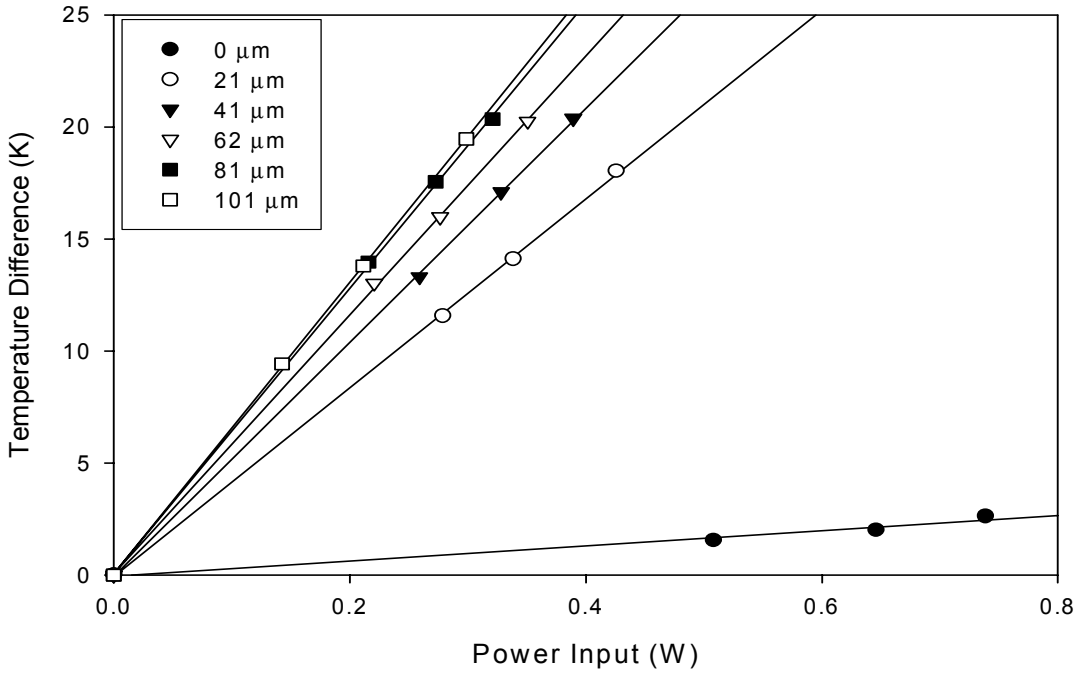

Temperature Differential vs Power Input for Mercury Droplet Array, in Xenon at Ambient Pressure, with Applied Load

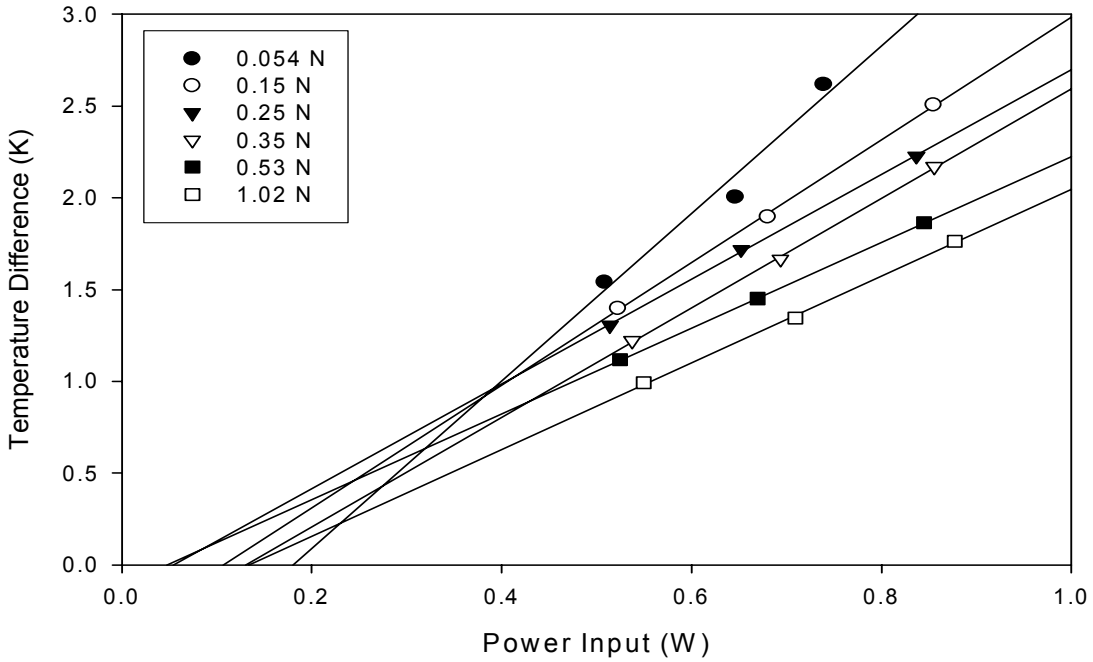

1600 Droplet Experiment in 0.5 torr Air

Distance	Delta T	Uncorrected Power	Load	Delta T	Uncorrected Power
(μm)	(K)	(W)	(N)	(K)	(W)
26.29	0.00	0.00	0.01	0.00	0.00
26.29	11.08	0.22	0.01	1.22	0.32
26.29	13.52	0.28	0.01	1.47	0.39
26.29	17.19	0.35	0.01	1.78	0.50
49.11	0.00	0.00	0.10	0.00	0.00
49.11	17.84	0.35	0.10	1.27	0.51
49.11	14.76	0.29	0.10	1.01	0.42
49.11	11.51	0.23	0.10	0.73	0.32
68.46	0.00	0.00	0.20	0.00	0.00
68.46	10.69	0.20	0.20	0.72	0.32
68.46	13.49	0.26	0.19	0.92	0.39
68.46	17.56	0.34	0.20	1.22	0.51
88.30	0.00	0.00	0.30	0.00	0.00
88.30	17.20	0.33	0.30	1.25	0.52
88.30	14.39	0.27	0.30	0.98	0.42
88.30	11.14	0.21	0.29	0.75	0.33
108.64	0.00	0.00	0.50	0.00	0.00
108.64	8.44	0.16	0.50	0.72	0.32
108.64	12.04	0.23	0.49	0.91	0.39
108.64	16.84	0.32	0.49	1.22	0.51
			0.98	0.00	0.00
			0.98	1.19	0.51
			0.98	0.94	0.42
			0.98	0.70	0.32

Temperature Differential vs Power Input for Mercury Droplet Array, Air at 0.5 torr, for Gap

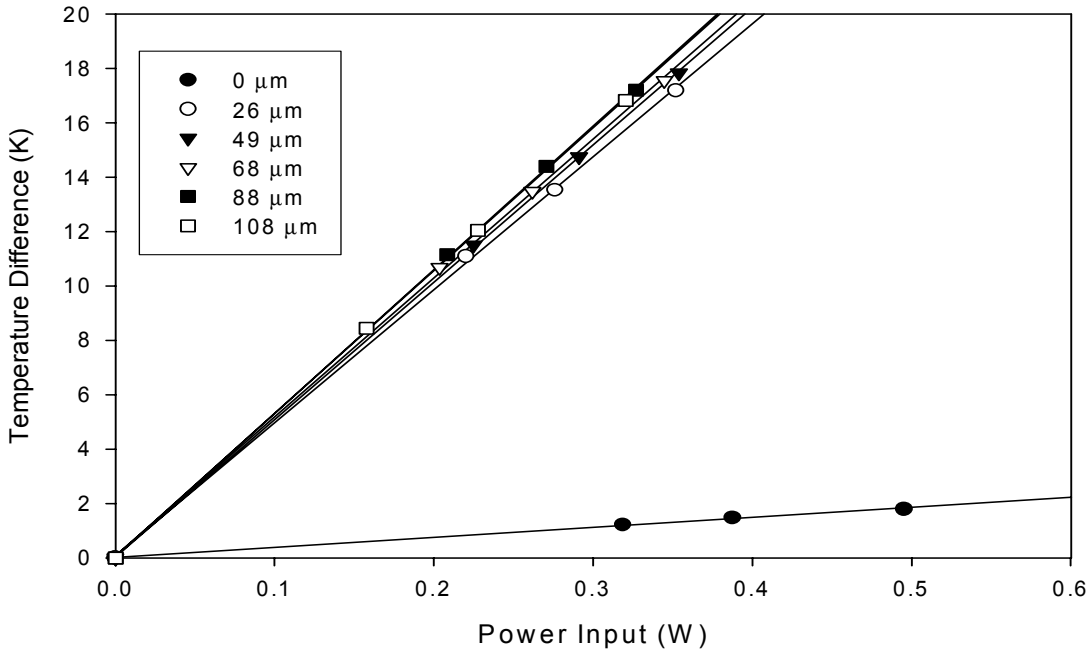

Temperature Differential vs Power Input for Mercury Droplet Array, Air at 0.5 torr, with Applied Load